Chemical Engineering Science 328 (2026) 123752

Contents lists available at ScienceDirect

Chemical Engineering Science

journal homepage: www.elsevier.com/locate/ces

NMR cryodiffusometry determination of pore utility differentials for liquid-phase diffusion within alumina, catalyst support pellets

Stefano Collins [a,b,c,d], Dina Lofficial [b], Séverine Humbert [b], Thibaud Chevalier [b], Christophe Vallee [b], Huw E.L. Williams [d], Galina E. Pavlovskaya [c], Thomas Meersmann [c], Sean P. Rigby [a,*]

[a] Department of Chemical and Environmental Engineering, Faculty of Engineering, University of Nottingham, University Park, Nottingham NG7 2RD, UK
[b] IFP Energies Nouvelles, Rond-point de l'échangeur de Solaize, BP 3, 69360 Solaize, France
[c] Sir Peter Mansfield Imaging Centre, University of Nottingham, University Park, Nottingham NG7 2RD, UK
[d] Centre for Biomedical Sciences, University of Nottingham, University Park, Nottingham NG7 2RD, UK

ARTICLE INFO

Keywords:
Thermoporometry
PFG NMR
Non-wetting phase entrapment
Critical path theory
Templating

ABSTRACT

Intelligent design of optimal void spaces for diverse applications of porous media remains a still outstanding objective. The aim here was to predict the tortuosity for liquid-phase diffusion within complex, bidisperse, porous alumina pellets, and, thereby, assess the degree of control achieved via a porogen-based synthesis. NMR cryodiffusometry was used as a novel means to implement the so-called "sifting strategy" to identify the key aspects of the void space to include in a more efficient, minimalist, pore structural model for materials unsuited to a "brute-force" modelling approach. The cryodiffusometry showed, through the particular mathematical form of the data obtained, that the predominant geometry of the void space was a random cluster, but also detected the presence of some "dead volume" that provided little, or no, apparent contribution to the overall mass transport. This particular feature of the void space was corroborated by applying the concept of bound volume index to mercury porosimetry retraction data. A minimalist model, constructed incorporating these two key aspects of the void space, was found to be fully predictive of mass transport rates of water, or cyclohexane, within the alumina pellets. Seeded percolation analysis of gas sorption scanning curves demonstrated the dead volume was associated with particular pore space regions with low accessibility, which was consistent with previous Monte-Carlo simulations of self-diffusion on random cluster models and TEM data. The theoretical framework involving a random cluster with dead volume provided a more comprehensive account of the diverse experimental findings than a complementary critical path analysis-based approach.

1. Introduction

A long-standing research question, in areas like reaction engineering, is how to predict mass transport rates within disordered porous media from structural characterization data (Rigby, 2020; Yang et al., 2024; Santos et al., 2022; Isaacs et al., 2019; Müllner et al., 2016; Ghanbarian et al., 2013; Bukowski et al., 2021; Holzer et al., 2023). For heterogeneous catalysts for diffusion-limited reactions there is a trade-off between providing as much surface area to disperse the catalyst as possible, normally requiring small pores, and achieving as high an effectiveness factor as possible, typically needing large pores, particularly in the Knudsen diffusion regime (Twigg, 2014). Many industrial catalyst supports are still disordered materials, such as alumina or sol–gel silica, because they are cheap and generally much more robust to thermochemical action under intensive reaction conditions than templated, ordered materials, which tend to sinter or disintegrate. There is a multiplicity of options for the control parameters in the various stages in the manufacture of amorphous aluminas, from initial precipitation, through pellet feed production, forming, and calcination. (Rigby, 2020; Twigg, 2014). All of these possible options can significantly impact the final pore structure of the pellet leading to multifarious, complex void spaces. Hence, there is a need for comprehensive pore structural characterization methods capable of assessing the particular complex features of each type of alumina.

The complex nature of amorphous porous materials means it is hard to know in advance how much characteristic information is required to

* Corresponding author.
E-mail address: sean.rigby@nottingham.ac.uk (S.P. Rigby).

https://doi.org/10.1016/j.ces.2026.123752
Received 11 November 2025; Received in revised form 5 February 2026; Accepted 7 March 2026
Available online 10 March 2026

make a successful prediction (Rigby, 2023). Two different main strategies have been adopted to address this problem. One is to attempt to achieve as complete a pore structural characterization as possible, typically using a three-dimensional imaging modality, such as computerized X-ray tomography (CXT), focused ion beam scanning electron microscopy (FIB-SEM), or electron tomography, and then use the image data itself as the basis of a structural model for conducting simulations of mass transport. There have been some successes with this so-called "brute-force" approach for suitable systems, such as the prediction of mass transport using lattice-Boltzmann simulations on a model of highly porous foam materials constructed directly from a CXT image (Pavlovskaya et al., 2018).

Unfortunately, a key issue with this strategy is that disordered porous solids often possess a hierarchical pore structure, or a wide range of pore sizes, that exceeds the range of resolution of a single imaging modality, or the field of view possible at the required resolution is smaller than the representative volume required to obtain a statistically reliable sample of the void space (Rigby, 2020; Rigby, 2023). A potential solution to this problem is to use multiple imaging modalities, such as combining CXT and FIB-SEM, such that, together, they straddle the required range of length-scales. For example, Yamada et al. (Yamada et al., 2021) imaged a particular batch of bimodal, alumina, catalyst support pellets, with electron tomography (3D-TEM) for a sample volume of 304 × 304 × 53 nm at a resolution of 7 nm to characterise the mesoporosity (modal pore size ~14 nm), and synchrotron X-ray nano-CT for a sample volume of 20^3 μm at a resolution of 35 nm to characterise the macroporosity (modal pore size ~461 nm). The images, thereby obtained, were then used to construct a hierarchical model of the porous solid at the corresponding length-scales. First, diffusion was simulated under a concentration gradient in the void space of a lower length-scale model derived from the 3D-TEM image, while the solid was considered impermeable. These simulations were used to determine an effective diffusivity for use as the continuum transport parameter for the "solid" phase in the larger length-scale model derived from the CXT image. Diffusion was then simulated on the larger length-scale model with transport permitted through both the macroporosity and the permeable solid phase. These simulations gave rise to excellent predictions of the observed, overall effective diffusivity for the alumina pellets, as measured experimentally using a Wicke-Kallenbach cell (Yamada et al., 2021). However, for this particular alumina, it should be highlighted that the much simpler random pore model of Wakao and Smith (Wakao and Smith, 1963), with the parameters for the model measured using mercury porosimetry, also gave rise to just as good predictions of diffusivity. These latter results suggest the pore structure of this particular alumina was relatively simple and homogeneous, and, therefore, the same approach may not work for the highly disordered void spaces of more complex, porous materials. Further, while, in this case, the imaged volumes were statistically representative of their respective length-scales, for some materials the correlation length exceeds the size of the pellet, and sufficient images at the necessary resolutions produce a data-set too large to manage with current computing power (Nepryahin et al., 2016). Hence, an alternative approach to the brute-force method is often required.

An alternative strategy, to the brute-force approach, is to explicitly identify the key aspects of the pore structure that control the mass transfer rate, and, thereby, construct a minimalist model that contains only those material characteristics essential to make the model predictive for the physical processes in question (Rigby, 2023). One approach to identify these key characteristics is the sifting strategy (Rigby, 2020; Rigby, 2023). This involves knocking-out particular aspects, or constituents, of the void space, such as pores in a particular bin of sizes, and testing the impact on a given mass transfer process. The relative importance of different components of the void space can then be assessed, and only the key aspects included in a model. This strategy can be implemented using a range of experimental techniques, including integrated nitrogen sorption and mercury porosimetry (Mousa et al., 2023a,b), or water pre-adsorption and hyperpolarised xenon-129 gas phase magnetic resonance imaging (MRI) (Hill-Casey et al., 2021). In this previous work, it was shown that, within tabletted methanol synthesis catalyst pellets, diffusional ingress of gas was controlled by surface clusters of large pores, while, for a wash-coated monolith, permeation of the structure was controlled by the unfilled macroporosity in the walls of channel corners. However, these previous techniques were more useful for the largest pores, and, so, a method applicable to a wider range of pore sizes is needed. In this work, the combination of NMR cryoporometry and PFG NMR, known as NMR cryodiffusometry (Filippov and Skirda, 2000; Perkins et al., 2008; Shiko et al., 2012; Kondrashova et al., 2011), will be used to "sift-out" the controlling aspects of the void space of bimodal alumina catalyst support pellets. Further, cryodiffusometry allows the direct testing of the incremental mass transport contributions from progressive additions of ever larger pores to the void space network.

Particular aspects of the void space of a disordered porous solid can control mass transport rates. Studies of steady-state permeation through porous pellets, using a Wicke-Kallenbach cell, have suggested the importance of so-called "transport pores" that carry the majority of the diffusive flux (Dullien, 1992). Previous work on boehmite γ-alumina catalyst supports, showed that the void space consisted of two levels of porosity, one associated with voids between individual alumina nanocrystals within aggregates of such crystals, and another associated with larger voids between these aggregates (Kolitcheff et al., 2017). For these materials, commonly-used, literature correlations of porosity and tortuosity enabled more accurate predictions of tortuosity if the porosity used in the correlation was only that corresponding to just the inter-aggregate voids, and not the total porosity, and, therefore, ignoring the intra-aggregate porosity. This work demonstrated a binary division between porosity that contributes substantially to diffusion, and porosity that does not. More recently, an attempt was made to define and measure a so-called "pore utility index (PUI)" that quantifies the relative usefulness of a given sub-set of pores to overall mass transport (Mousa et al., 2023). In this work, it will be shown that different sets of pores make dramatically different-sized contributions to mass transport, and these can be identified and quantified.

Mercury porosimetry is a commonly used and powerful technique for pore structural characterisation (Van Brakel et al., 1981; Giesche, 2006). Structural hysteresis is often associated with entrapment, where some residual mercury remains at the end of the experiment when the pressure is reduced back to atmospheric. Experiments with glass micromodel experiments suggest that entrapment is associated with "snap-off" of the mercury meniscus when it is required to exit from wide pore bodies through neighbouring narrow necks, or when there is the presence of heterogeneities such as vugs, or large scale correlations in the spatial distribution of pore sizes such that "islands" of large pores are shielded by a surrounding "sea" of much smaller pores (Wardlaw and McKellar, 1981; Tsakiroglou and Payatakes, 1998). The places in void spaces of water-wetting, oil reservoir rocks where mercury gets entrapped are typically also the places where oil gets left behind following secondary recovery methods (Appel et al., 1998). Hence, mercury porosimetry is often used to predict bound volume index (BVI), which is the residual fraction of the original oil-in-place that is left behind following secondary recovery, for oil reservoir rocks. This is because both oil and mercury tend to get left behind in the same places in the void space, being those with low accessibility due to low pore connectivity and high shielding of wider voids by narrow necks. These regions are also associated with slower exchange of water in diffusion experiments. Hence, by analogy with the oil industry, in this work the mercury entrapment will be used as a tracer for regions of the void space with low accessibility and poor exchangeability of fluids, henceforth referred to as "dead voidage".

As briefly mentioned above, macropores are added to mesoporous catalyst supports to provide more ready access of reactants to the interior surface area. A variety of fabrication methods are possible, but, in this work, a porogen will be used to induce macroporosity into the

mesopore network, via a method that is described in more detail below and elsewhere (Collins et al., 2026). An approach based upon percolation theory and critical path theory (CPT) will be used to assess whether the chosen method of introduction of macroporosity improves the critical pore size controlling mass transport.

The overall aim of this work is to predict the tortuosity for liquid-phase, molecular regime diffusion within porous alumina catalyst support pellets and, thereby, assess the impact of the addition of macroporosity on liquid-phase molecular diffusion. Electron microscopy will be used to image the typical morphology of the alumina pellets. NMR cryodiffusometry studies will determine void space descriptors, such as the overall pore size distribution, and also the basic geometric form of the mesopore network, and assess the contributions of individual bins in pore size to mass transport rates. Mercury porosimetry will also distinguish between pores making substantial versus negligible contributions to observed mass transport rates. Percolation analysis of gas sorption scanning curve data and TEM will be used to understand why different sets of pores make different levels of contribution to diffusion.

2. Theory

2.1. Mercury porosimetry

Even fully-equilibrated, raw mercury porosimetry data typically exhibits hysteresis between the intrusion and extrusion curves. This hysteresis is generally considered to have two main causes, namely contact angle hysteresis and structural hysteresis. It is well known (Van Brakel et al., 1981) that both the surface tension γ and contact angle θ can change with the radius of curvature of the meniscus *r*, and that the contact angle varies depending upon whether the meniscus is advancing or receding. The raw data from mercury porosimetry is often analysed using the longstanding Washburn (Washburn, 1921) Equation:

$$r = \frac{-2\gamma cos\theta}{p_{Hg}} \tag{1}$$

More recently (Kloubek, 1981; Rigby, 2000) correlations for the product γ cosθ have been introduced that take these aforementioned effects into account. These correlations have been derived by calibrating the pressure p_{Hg} at which mercury enters or leaves a series of controlled pore glasses, used as model porous media with a regular structure, against an independent measure of pore size *r*, which in this case was electron microscopy (Liabastre and Orr, 1978). Insertion of these correlations into the Washburn Equation gives rise to expressions of the form:

$$r = \frac{-A + \sqrt{A^2 - 2p_{Hg}B}}{p_{Hg}} \tag{2}$$

where A and B are constants depending on the material, and whether the mercury meniscus is advancing or retreating. The values of A and B for alumina are given in Table 1. The expressions of the form of Eq. (2) are empirical in origin, and are, therefore, of limited range of applicability (see Table 1), and also contain experimental error (~4–5%)(Kloubek, 1981).

Table 1
Parameters for use in Eq. (2).

Material	A.10^3/(N. m^{-1})	B.10^{12}/(N)	Range of validity/(nm)
Alumina (advancing meniscus)	−302.533	−0.739	6–99.75
Alumina (retreating meniscus)	−40	−240	4–68.5

2.2. Cryoporometry (or thermoporometry)

Cryoporometry can be used to determine pore sizes because, when located within confined geometries, the melting and freezing points of fluids are depressed below the value for bulk fluid by an amount inversely proportional to the characteristic dimension of the pore. The observed relation between the melting point depression ΔT_m and the characteristic pore size *d* is typically known as the Gibbs-Thomson equation (Petrov and Furó, 2006):

$$\Delta T_m = \frac{k}{(d - 2t)}, \tag{3}$$

where *k* is a constant of proportionality that depends upon the properties of the probe fluid, and *t* is the thickness of a thin layer of fluid immediately neighbouring the solid surface which does not freeze for most systems (Petrov and Furó, 2006; Schreiber et al., 2001; Jia et al., 2025). The typical cryoporometry experiment involves completely freezing the probe fluid within the cores of the pores within the sample, then progressively raising the temperature in small discrete steps (in NMR methods), or as a slow ramp (in differential scanning calorimetry (DSC) methods), and determining the volume of probe fluid melting at each temperature. The Gibbs-Thomson equation can then be used to relate the observed melting temperature to the pore size, whilst the corresponding volume of pores is obtained from the amount of probe fluid melting. The amount of probe fluid that melts can be determined either from a change in the NMR signal intensity when using a relaxation time filter to distinguish solid from liquid, or using the heat-flow, arising from the latent heat of fusion, measured by differential scanning calorimetry (DSC) (Bafarawa et al., 2014).

2.3. Pulsed-field gradient (PFG) NMR diffusometry

The PFG NMR experiments were performed with a stimulated echo pulse sequence (see Section 3.2.7) and so the data were fitted to the log-attenuation equation (Rigby, 2020):

$$ln(\psi) = \ln\left(\frac{I}{I_0}\right) = -(\gamma\delta G)^2\left(\Delta - \frac{\delta}{3}\right)D_{PFG} \tag{4}$$

where *I* is the experimental observed intensity, I_0 is the intensity with no attenuation, γ is the gyromagnetic ratio, δ is the gradient pulse duration, *G* is the gradient strength, Δ is the diffusion time and D_{PFG} is the fitted diffusivity

Combined NMR cryoporometry and diffusometry is known as cryodiffusometry. In partially-molten samples, during cryodiffusometry, the region of void space explored by a given diffusing, liquid molecule may be disconnected and of limited spatial extent (size $\sim V/S$) due to confinement between remaining ice 'walls'. When the root-mean-square (rms) displacement of a diffusing molecule is of a similar length-scale to that of the molten region that it is exploring, then the apparent measured diffusivity depends upon the distance between ice walls. At very short diffusion times, the molecules do not interact with the ice walls at all (and the observed diffusivity D_0 will be that intrinsic to the pore space network), but, as the diffusion time increases, ever more molecules will eventually interact with the ice walls, and, thereby, have their ultimate displacement curtailed. By analogy with the suggestion from the literature for finding the intrinsic diffusivity within finite grains, the apparent diffusivity D_{PFG} observed would then be a function of the diffusion time, Δ, given by (Mitra et al., 1993; Gjerdåker et al., 1999):

$$D_{PFG}(\Delta) = D_0 - \frac{4D_0^{3/2}S}{9\pi^{1/2}V}\Delta^{1/2} \tag{5}$$

where S/V is the outer surface area-to-internal volume ratio of the molten region. According to Eq. (5), if the apparent diffusivity, for partially-molten systems under diffusional restrictions, is measured for

increasing values of diffusion time, then it will appear to decrease.

Cryodiffusometry allows the individual contributions, to the overall observed mass transport rate, of ever larger pores progressively added to the network of molten (conducting) pores, to be determined. The contributions to mass transport of the various different parts of the void space are assessed in a direct way, as they are actively "knocked out" of the wider network by freezing, and the explicit difference they make, as they are progressively re-introduced, assessed. The cryodiffusometry experiments will be performed with water as the probe fluid, since the phase transitions within mesopores for water are more simple than for hydrocarbon liquids, as the latter often have a more complicated phase transition, involving phenomena such as so-called "mushy-ice" phases (Rigby, 2020; Dore et al., 2004). However, if the surface of the porous material is polar, then the relative stronger interactions with water, than for non-polar organic liquids, can make the apparent tortuosity vary with probe fluid. In order to test the size of this potential effect the tortuosity for water in a fully-molten sample will be compared with that for cyclohexane. Previous work involving the triangulation of pore sizes with mercury thermoporometry and gas adsorption has shown that the freezing of water in mesopores in oxide materials during cryoporometry involves complete solidification of the pore core, except for the non-freezing layer (Mousa et al., 2022).

2.4. Percolation analysis

The general accessibility of a pore network can be assessed using percolation theory and quantitatively estimated using a connectivity parameter, *Z,* for a model lattice representing that network. Since gas desorption is supposed to be an invasion percolation process, then gas sorption data can be used to determine the effective network connectivity (Seaton, 1991; Gregg and Sing, 1982; Parlar and Yortsos, 1988; Kikkinides and Valiullin, 2023; Söllner et al., 2024). In a percolation analysis of gas desorption, the occupied elements of the model lattice are those that are below their critical pressure for desorption (according to the Kelvin equation (Gregg and Sing, 1982)) and could potentially contain vapour. If only the degree of accessibility of a sub-set of pores is required, then gas sorption scanning curves can be used to determine the connectivity in conjunction with a seeded percolation model that takes into account the pores left empty at the top of the scanning curve. Parlar and Yortsos (Parlar and Yortsos, 1988) provided the accessibility function P_b for seeded percolation based upon a Bethe lattice (or Cayley tree) of pore bonds, where the fraction of pore bonds actually occupied at a given relative pressure is given by:

$$P_b(p;p_i) = p - (p-p_i)\frac{(1-p)^{2(Z-1)}}{(1-x)^{2(Z-1)}} \tag{6}$$

where p is the fraction of pore bonds allowed to be occupied, and p_i is the fraction of pore bonds that were left occupied by vapour at the top of the scanning curve, and so were the so-called seeds for percolation. The parameter x is obtained from the solution of the formula (Parlar and Yortsos, 1988):

$$x(1-x)^{Z-2} = (p-p_i)(1-p)^{Z-2} \tag{7}$$

The connectivity parameter can be obtained from a fit of the theoretical accessibility function to the experimental gas sorption data. However, it is noted that the percolation formulae are expressed in terms of pore number fractions whereas gas sorption data deliver pore size distributions weighted by pore volume. Hence, to use gas sorption data for percolation analysis, it is also necessary to make an assumption about the relationship between pore diameter (d) and pore length (l) so that incremental volumes of pores of a given diameter can be converted into pore numbers. In this work, the power law relation used in previous work will be used such that (Rigby et al., 2004):

$$l = kd^{\alpha} \tag{8}$$

where l is a constant and α is the power law exponent.

The Bethe lattice is used here as a mathematical model and, so, it is not claimed that the void space of the real materials studied here is exactly like a Bethe lattice. However, it is likely that a trend in the connectivity descriptor in the model will be reflected in that for the real material.

2.5. Critical path theory

Two theoretical frameworks will be used to interpret the data in this work. In the first, the data from the NMR cryodiffusometry and mercury porosimetry will be interpreted in terms of the critical path theory (CPT), originally developed by Ambegaokar et al. (Ambegoakar et al., 1971), but as described by Friedman and Seaton (Friedman and Seaton, 1998). In CPT, mass transport in an inter-connected network is effectively controlled by a critical pore size. In the cryodiffusometry experiment the pore network is initially fully frozen (except for non-freezing surface layer) and molten pores are 'added back' into the network in order of increasing size, and, thus, increasing conductance, since, in molecular diffusion, conductance is proportional to the square of the pore diameter (Friedman and Seaton, 1998). According to the formulation of CPT of Friedman and Seaton (Friedman and Seaton, 1998), in such a case, since the pores melting initially will have lower conductance than the eventual critical pore, they will be *effectively* added in parallel with each other, and, thus, the observed conductance should increase (and, thence, the corresponding tortuosity decrease) until the critical pore is reached. Thereafter, since the conductances of the subsequent melting pores will be higher than the critical pore, these pores are, in contrast, *effectively* added to the network in series with the critical pore, and so their resistance can be neglected. This reasoning suggests that the critical pore size, controlling mass transport in a given network, will be associated with a sharp transition (a "knee") in the trend (slope) of the tortuosity with increasing molten pore size.

CPT further suggests that the critical pore size corresponds to the percolation threshold of the network, and, thereby, CPT is linked to percolation theory (Ambegoakar et al., 1971; Friedman and Seaton, 1998). In the case of the entrapment of a non-wetting phase (nwp) within porous media, percolation theory is concerned with predicting whether the clusters of pores filled with nwp at a given saturation (fractional occupancy) of nwp remain connected, such that there is at least one pathway from any pore filled with nwp, only passing through other pores filled with nwp, to the surface of the porous solid. As the saturation of the nwp decreases, there will be a certain saturation where the fraction of pores filled with nwp becomes such that it becomes disconnected which corresponds to the percolation threshold. For relatively simple systems, the residual saturation (entrapment) when the nwp becomes disconnected corresponds to the percolation threshold (Larson et al., 1981). Hence, during mercury retraction in porosimetry, the saturation of the nwp is steadily decreasing, and the onset of entrapment will ensue once it reaches the percolation threshold. Therefore, the onset of entrapment will identify the critical pore size since this corresponds to the percolation threshold. This reasoning predicts that the pore size for the onset of mercury entrapment will match the pore size at which the trend in cryodiffusometry tortuosity changes markedly.

2.6. Random cluster (RC) structural model

The second theoretical framework involves a pore structural model with a given effective porosity. The random cluster (RC) is a type of structural model with a random distribution of impermeable solid phase (Elias-Kohav et al., 1991). A random cluster is constructed on a cubic site lattice, where the sites in the lattice are allocated completely randomly to either solid or void phase, such that the eventual overall fraction of void spaces equals the desired porosity. The complete randomness of

allocation means that solid sites may be immediate neighbours, and potentially grow into a percolating network. Elias-Kohav et al. (Elias-Kohav et al., 1991), using the whole object averaging method, and Wakao and Smith (Wakao and Smith, 1963) via a different methodology, both showed that the tortuosity τ of a 3D random cluster is related to the porosity ε by:

$$\tau = 1/\varepsilon \tag{9}$$

In this work, this expression for tortuosity will be modified to take into account that only some of the whole pellet porosity (ε_{total}) is useful for mass transport, while a fraction f_{dead} of the pellet porosity is considered "dead volume", since it does not contribute significantly to the observed mass transport. It will be seen that this dead volume can be associated with the entrapped mercury with a fractional saturation of f_{Hg}. In such a case the tortuosity is given by:

$$\tau = \frac{1}{\varepsilon_{useful}} = \frac{1}{\varepsilon_{total}(1 - f_{dead})} = \frac{1}{\varepsilon_{total}\left(1 - f_{Hg}\right)} \tag{10}$$

3. Materials and methods

3.1. Materials

The materials studied in this work are alumina catalyst support pellets, produced specifically for this project by IFPEN. The pellets have been fabricated via a synthesis method in which differing amounts of a porogen were used to induce variable amounts of macroporosity (Lakshmi et al., 2022). The first step consists of forming a dispersion of boehmite powder in water by use of a dispersing additive, such as an inorganic acid, and mixing. A porogen, such as a refined oil, is added to this suspension in the form of an emulsion using a surfactant (Deshmukh et al., 2018; Dong et al., 2022). The porogen acted as a template to create macropores and was then removed by calcination. The resultant pellets were either mesoporous only (A), or bidisperse mesoporous and macroporous (the rest). The different batches used in this work are listed in Table 2. The four batches studied here were chosen as they cover a wide range in porogen content.

3.2. Methods

The basic physical principles and general experimental procedures underlying the various experimental characterization methods used here are described in more detail elsewhere (Rigby, 2020). This section will thus only provide details more specific to the particular experiments conducted on the samples studied here.

3.2.1. Scanning electron microscope

The samples were prepared by vacuum impregnation with a highly fluid monomer (methyl methacrylate), followed by its in-situ polymerisation. The polymerisation was carried out under controlled temperature and pressure in an autoclave, producing solid blocks in the form of cylinders. The samples were then polished with a rotary polisher (Eco-Met 250) using SiC polishing disks of reference P4000, which is equivalent to a granulometry of roughly 5 μm. The images were taken on a Zeiss SUPRA 40. The 2D images were then processed, using the 'plug im!' software, to output a PSD histogram and a porosity (assuming isotropy in 3D) for each batch.

Table 2
Details of batches of alumina catalyst support pellet used in this work.

Batch identifier	Relative porogen content/arb. units
A	0
B	21
C	56
D	84

3.2.2. Transmission electron microscope

For the 'cross-sectional' preparation, the sample was first embedded as chips (powder form) in epoxy resin. Subsequently, sections of 70 nm thickness were taken using a high precision ultramicrotome. These sections were placed on the TEM support (5 mm diameter grid). For the 'direct' preparation, the sample was first ground in a mortar and then a spatula tip of the powder was ultrasonically dispersed in ethanol. A drop of the mixture was then placed on the TEM support. The sample was then observed in bright field TEM mode on a JEOL F200 microscope.

3.2.3. SAXS

Small angle X-Ray scattering (SAXS) was performed on the SWING beamline of the synchrotron SOLEIL (Saclay, France) with an 8 keV incident beam. Both spherical pellet (between Kapton foil) and pelletised (powder) form of the γ-alumina were analysed. For the pelletised form, the crushed, powdered samples were pelletised under pressure (1.5 tonnes), forming cylindrical pellets, of 13 mm in diameter and approximately 300 μm in thickness. To cover a wide range of q values, two sample-detector distances (1003 mm and 6229 mm) were employed. The scattering images were recorded using an AVIEX PCCD170170 detector.

3.2.4. Nitrogen sorption

Nitrogen physisorption was carried out at 77 K on a 3Flex instrument (Micromeritics). Before any experiment, the samples were subjected to pre-treatment under a secondary vacuum (10^{-5} mbar) at 350°C for 3 h to remove any impurities, and physisorbed and chemisorbed water. The pore volume and BET surface area were determined from the nitrogen isotherm. The pore size distributions were determined from the nitrogen adsorption isotherm branch based on the Barrett-Joyner-Halenda (BJH) method, using the hemispherical meniscus in the Kelvin equation, and the Harkins-Jura *t*-layer equation (Rigby, 2020; Gregg and Sing, 1982).

3.2.5. DSC thermoporometry

The experiment was carried out using a DSC Q10 V9.8 machine equipped with a cooling apparatus and a data processing system, which was used to measure the melting curves. The sample is initially cooled to 235 K to ensure all the freezable water is frozen. Then the melting curve was measured. A preliminary study determined the ramp rate needed for DSC thermoporometry to be 0.3 K min^{-1} to ensure the optimal balance between sensitivity and signal-to-noise. The DSC can measure heat flow rates with a resolution of ±0.5 μW and an accuracy of ±2 μW.

3.2.6. NMR cryoporometry

The samples were saturated with deionised water by immersion for 30 min in a beaker and then transferred to an NMR tube, having removed excess water on a wet piece of tissue paper. A wet piece of tissue paper was placed inside the tube, at the top, to ensure a humid environment during the experiment. The experiments were undertaken on a Bruker Avance 3, 600 MHz with a BBFO (Broad Band Fluorine observe) Probe. A BCU2/BCU-Xtreme chiller unit with compressed air that is dried to a dew point of – 90°C was used, in combination with a stream of hot dry gas, to control the temperature of the sample. The dry air is then blown onto the sides of the tube to remove potential temperature gradient effects in the tube. For any NMR cryoporometry/cryodiffusometry experiment, the temperature was first decreased to 235 K for 30 min to ensure that all freezable water was frozen. The temperature was then progressively increased to 255 K. From there, the temperature was increased to 278 K in increments of 0.2 K. Equilibration times of 15 min at each temperature were ensured to allow the system to settle before measuring the NMR signal. The correct echo time was carefully selected so that the solid ice signal decayed to an undetectable level, while the signal for the liquid was retained (echo filter) (Petrov and Furó, 2009). The average measured relaxation time, T_1, was approximately 0.6 s, whereas the echo filter time was 0.2 ms.

3.2.7. Pulsed-field gradient (PFG) NMR

The PFG NMR experiments were performed with a stimulated echo pulse sequence. The data were processed using Topspin software. The 90-degree pulse length was 10.9 μs. The delay between the first two such pulses was 200 μs, as was the same delay parameter (D16 in Topspin) used elsewhere in the pulse sequence. For each diffusion experiment, 16 data points were taken at increasing gradient strengths from 3.4 to 32.4 G cm^{-1}, and each point was obtained with 32 scans or higher depending on the signal strength. The experiments were performed with five different diffusion times (Δ) ranging from 0.1 to 0.5 s at each temperature (at low temperatures only high big deltas could be used to obtain a suitable attenuation). These Δ values have been selected, as they are shorter than the spin–lattice relaxation time of liquid water (approximately 0.6 s, see Appendix), while still providing a broad experimental range for analysis. For each diffusion time, the gradient pulse duration, δ, needs to be calibrated to acquire data that covers the entire attenuation curve region, down to 5%. In other words, the last PFG-echo intensity needs to be 5% of the first PFG-echo intensity, in order to cover a wide range in intensities to get a good quality fit. Experiments were conducted with either water or cyclohexane as the probe fluid to investigate whether the tortuosity values obtained were affected by differences in surface-molecule interactions.

3.2.8. Mercury porosimetry

The pellets were analysed by mercury intrusion porosimetry using an AUTOPORE IV instrument (Micromeritics). The equilibration time at each pressure was set to 30 s or 100 s. Before analysis, the samples were subjected to a pre-treatment at 250°C for 2 h in an oven.

4. Results

4.1. Scanning electron microscopy

Fig. 1 shows typical SEM images of pellets from Batches A-D. It can be seen that, as the porogen content increased, so did the volume fraction of macroporosity.

The particular macroporosities for batches B-D were obtained from image analysis of several images like those in Fig. 1, and the relevant values are shown in Table 3. Image analysis was also conducted to obtain the average pore size of the macropores and these are given in Table 3.

4.2. Transmission electron microscopy

Fig. 2 shows TEM images for batch D that demonstrate that the arrangement of the alumina platelets around the macropores and the arrangement of the platelets deep inside the matrix are different. The image of the interior of the mesoporous matrix shows random clusters of alumina platelets (or crystallites) within that matrix. The platelets typically have a thickness of ~2.5–4 nm and a length of ~7–20 nm. The image of the boundary region around the macropore shows that the platelets tend to have a nematic-like arrangement there, whereby there is a local 1-dimensional, regular array of alumina platelets along the boundary of the macropores. In the TEM image of the macropore boundary, long dark lines corresponding to long pores can be seen formed between the aligned platelets. In contrast, no discernible regular pattern is seen in the platelets in the matrix. Similar findings were also obtained for batches B and C.

4.3. SAXS

Fig. 3 shows the SAXS data for powdered samples from Batches A-D. It can be seen that the curves for all batches are superposed at large values of q down to ~0.03, corresponding to a length-scale of ~3 nm, which is the same as the typical thickness of the platelets from TEM. Thereafter, they diverge with the steepness of the curves increasing in

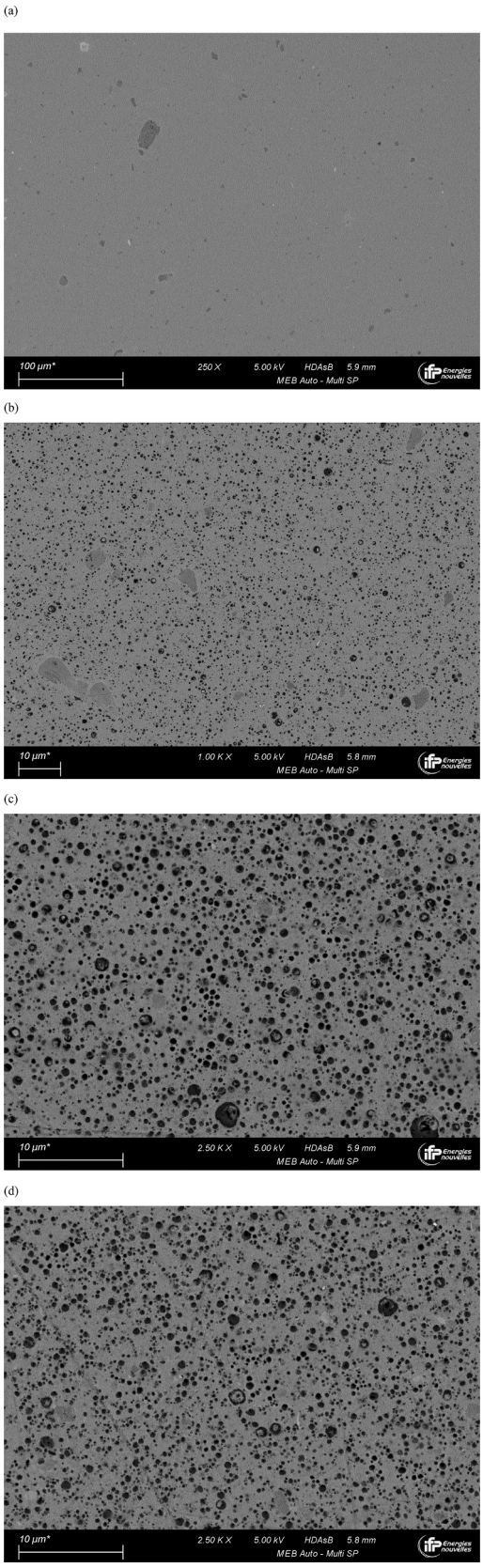

Fig. 1. Typical SEM images of pellets from batches (a) A, (b) B, (c), C, and (d) D.

Table 3
Results of the analysis of SEM images of batches A-D.

Batch	Macro-porosity from SEM	Average macropore size/μm
A	0.0	N/A
B	0.09 ± 0.01	0.28
C	0.18 ± 0.02	0.30
D	0.20 ± 0.01	0.28

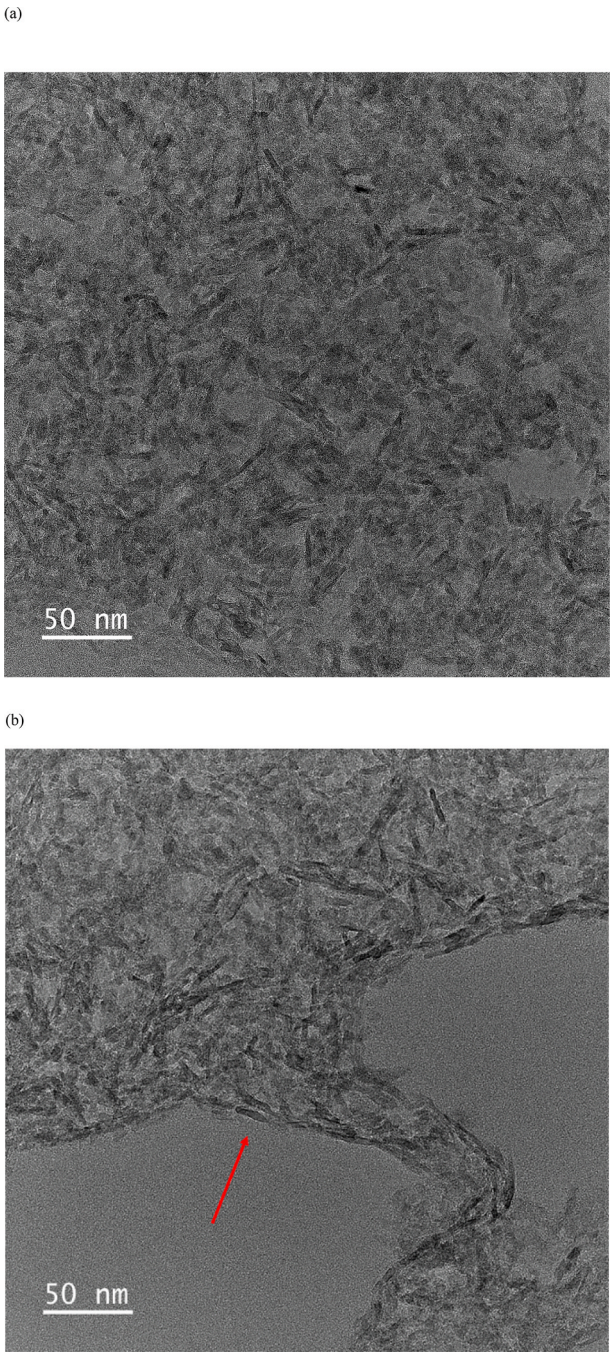

Fig. 2. (a) Cross-sectional TEM image of the internal mesoporous matrix region of a pellet of batch D showing the random arrangement of platelets in the matrix. The scale bar is 50 nm. (b) Cross-sectional TEM image of a region around macropores within a pellet from batch D showing the nematic arrangement of platelets around macropores. The red arrow indicates a region of aligned platelets (Collins et al., 2026).

the order A-D. For values of q below ~0.005 the curves begin to converge again. On the log–log plot there are three linear regions for q-values above ~0.08, below ~0.005, and between ~0.03 to ~0.1 but this varies between batches with the shortest intermediate linear region for Batch A. The transition zones between the linear regions on the log–log plot reflect structural transitions in the materials. The transition where the curves for the different batches also begin to diverge reflects the size of the thickness of the alumina platelets, and a transition from the surface roughness of the individual platelets to the aggregates of platelets. The second transition at larger length-scale (smaller q) reflects the hierarchy of packing of the aggregates probably responsible for the median pore size network.

4.4. Gas sorption

Nitrogen sorption scanning curves were obtained up to ultimate pressures of 0.85–7 and 0.96 for samples from Batches B-D, and an example data-set for Batch B is given in Fig. 4. From Fig. 4, it can be seen that the gas adsorption isotherm up to a relative pressure of 0.96 plateaus at the top, thereby indicating that the mesopore network fills completely and there is a gap in pore sizes between the largest mesopores and the macropores, since the macropores are left unfilled with condensed nitrogen. Similar results were obtained for Batches C and D. The PSD for the whole mesopore network was obtained from the nitrogen adsorption isotherm up to a relative pressure of 0.96 using the Barrett-Joyner-Halenda (BJH) algorithm and the Kelvin equation for a hemispherical meniscus with a t-layer correction (Rigby, 2020). The gas sorption PSDs have been presented in previous work (Collins et al., 2026).

The seeded percolation model of Parlar and Yortsos (Parlar and Yortsos, 1988) was then fitted to the nitrogen sorption scanning curves to relative pressures of 0.85–7 and 0.96, with the connectivity Z, the macroporous seed fraction, and the pore length power law exponent α as free-fitting parameters. An example of the fit of the experimental data for Batch B to the accessibility function is shown in Fig. 5. The results of the fits to all the scanning curves for Batches B-D are shown in Table 4.

From Table 4, it can be seen that the apparent model connectivity increases for scanning curves to the lower relative pressure, when compared with that for the scanning curves to the higher relative pressure. The lower pressure scanning curve only fills pores up to a diameter of ~14 nm, whereas the higher pressure curve fills pores up to a diameter of ~50 nm. The difference in apparent connectivity between the two reflects differences in the relative accessibility of the smaller pores filled in the lower pressure curve compared with the larger pores also filled in the higher pressure curve. The significance of this finding will be considered in the Discussion Section 5.

4.5. Comparison between NMR cryoporometry and DSC thermoporometry

Fig. 6 shows examples of the raw cryoporometry melting curves for Batches A-D. The curves have been corrected for the Curie effect and renormalised to the maximum signal intensity at the end of bulk melting. From Fig. 6, it can be seen that Batch A is solely mesoporous, with a single step that plateaus before 270 K. In contrast, the two steps in the curves for Batches B-D correspond to the mesoporosity, at the lower temperatures, and macroporosity, at the higher temperatures above 270 K. The relatively horizontal plateau between the two steps reflects that the mesopore and macropore sizes are relatively segregated.

In order to validate the calibration procedure mentioned in the Methods section, the PSDs obtained from the NMR cryoporometry melting curves were compared with those from DSC thermoporometry, and an example for Batch A is shown in Fig. 7. Equivalent data-sets for Batches B-D are included in the Supplementary Material Fig. S1. It can be seen that there is good agreement between the two techniques, suggesting that the results obtained are independent of the technique.

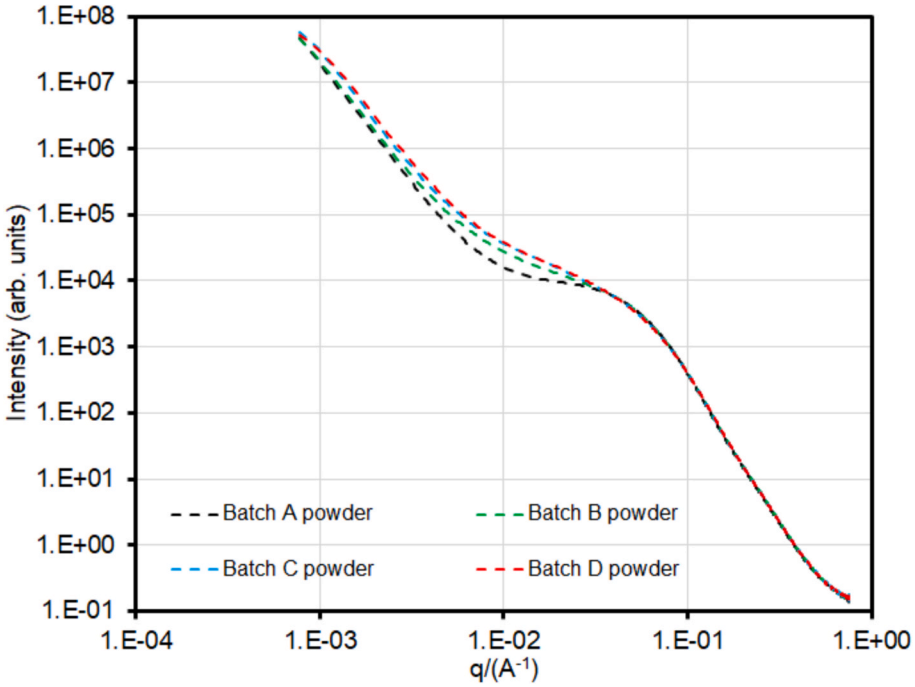

Fig. 3. SAXS data for powdered samples from Batches A–D.

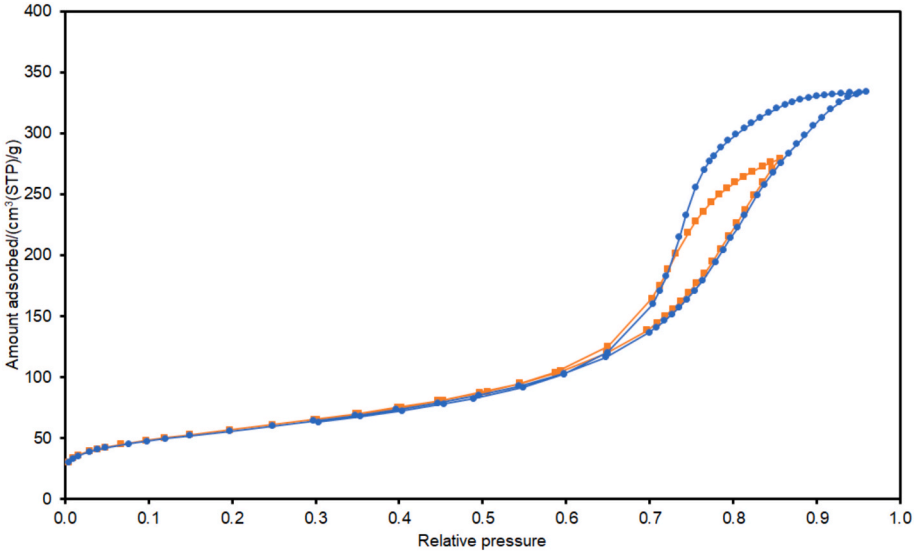

Fig. 4. Gas sorption isotherms up to ultimate relative pressures of 0.96 (●) and 0.85 (■) for a sample from Batch B.

4.6. NMR cryodiffusometry

As mentioned above, PFG-NMR experiments are performed with five different diffusion times (Δ) ranging from 0.1 to 0.5 s at each temperature. An example of a raw log-attenuation plot is given in Appendix A. The log-attenuation plots typically showed some curvature, and, thence, were fitted to a two-component model (Hollewand and Gladden, 1995). In subsequent analysis, given that the first fast component was predominant (typically >94%), then it was the one used in all subsequent analysis. Further, as described in the Theory section, since some of the samples were partially molten, then the diffusion might be potentially restricted. Hence, the data for different diffusion times at a given temperature were fitted to the model of Mitra et al. (Mitra et al., 1993), in order to obtain the limiting unrestricted diffusivity. An example of such a fit is given in the Appendix. The tortuosity factors subsequently given below were obtained from the limiting unrestricted diffusivity at zero diffusion time. For the typical data-set given in Fig. A2, the rms displacements ranged from ~10–25 μm. As can be seen from Fig. 1, this length-scale is larger than the typical distances between macropores.

Fig. 8 shows plots of PFG NMR tortuosity against molten fraction for batches A-D. Each plot shows the data from 3 separate samples, with 3 different sets of pellets. It can be seen that the results are repeatable between different samples from the same batch. The data cover different ranges of molten fraction for each batch because the range where data can be obtained requires that the diffusion is sufficiently unrestricted that molecules can move a sufficient distance down the applied gradient in order to give rise to detectable attenuation. The plots for all batches have an overall primary trend of a decline in tortuosity with increasing molten fraction. However, closer inspection of the data for each batch also reveals a fine structure that suggests differences between batches.

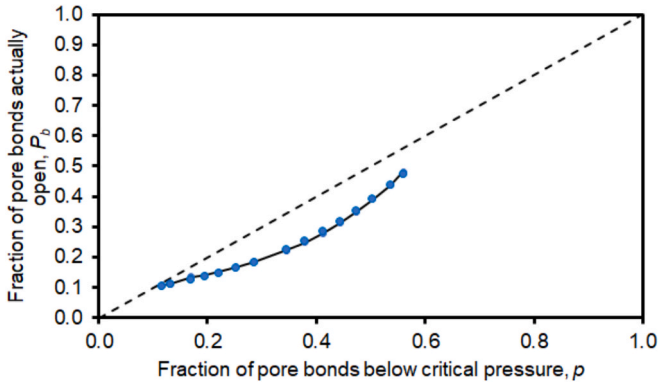

Fig. 5. Fit of the experimental gas sorption scanning curve (to relative pressure of 0.85) data for Batch B (●) to the accessibility function (solid line) for seeded percolation (Parlar and Yortsos, 1988).

Table 4
Results of the fit of the seeded percolation model (Parlar and Yortsos, 1988) to nitrogen sorption scanning curve data for Batches B–D.

Batch	Ultimate relative pressure of upper loop	Pore connectivity	Ultimate relative pressure of upper loop	Pore connectivity
B	0.96	2.26	0.85	2.87
C	0.96	2.29	0.85	2.89
D	0.96	2.24	0.87	3.30

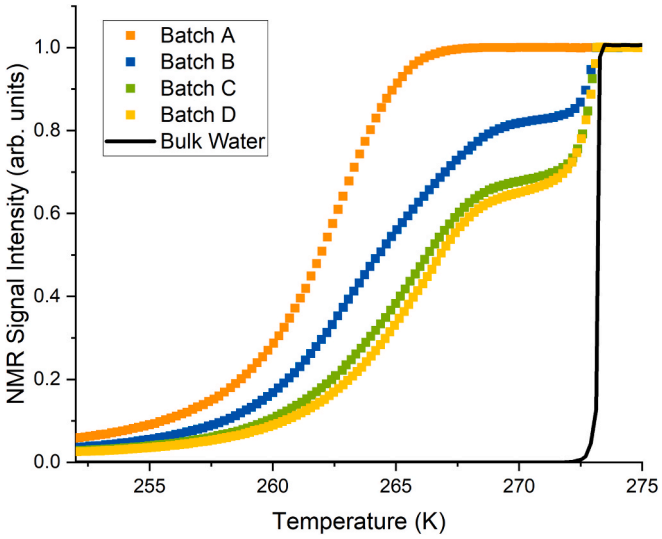

Fig. 6. NMR cryoporometry melting curves for bulk ice (solid line) and ice contained within the porous network of the alumina batches A, B, C and D.

From Fig. 8, it can be seen that the overall steep decline in tortuosity is interrupted for certain intervals in molten fraction for batches C and D. There is a noticeable pause in the decline over molten fractions of ~0.4–0.5 for both batches.

The general forms of the plots for batches A-D can be compared more directly by the construction of a universal plot where the reduced tortuosity (defined here as the ratio of tortuosity at a given molten fraction, τ, to that for a fully molten sample, τ_0) is plotted against molten fraction, as in Fig. 9. Further, given that the effect of specific surface interactions on tortuosity for a particular molecule is expected to be multiplicative, the reduced tortuosity should just retain the structural tortuosity component. From Fig. 9, it can be seen that, for the range of molten fractions for which data is available for all four batches (molten fraction >0.8), the four curves are well superposed upon each other. Further, the form of the data in the universal plot in Fig. 9 may also suggest that the aforementioned pause, or plateau, in the variation of tortuosity with molten fraction may extend from molten fractions below ~0.6 to ~0.47 for batches B-D, and on down to a molten fraction of ~0.4 for C and D. Thereafter there is a steep rise in tortuosity for batches C and D.

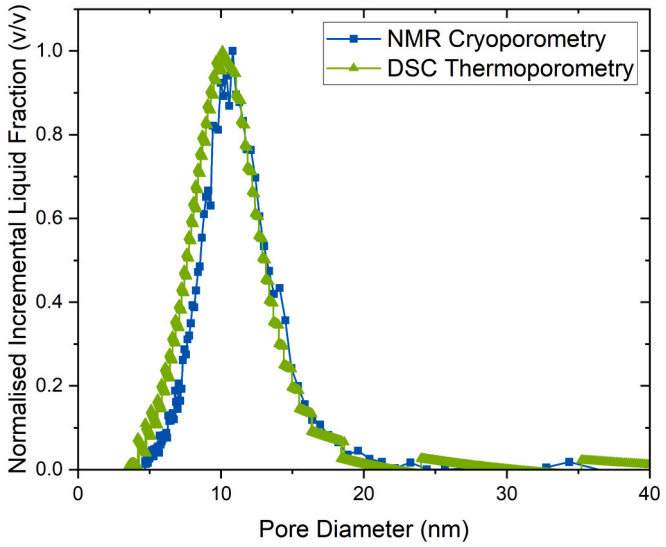

Fig. 7. Normalised incremental liquid fraction (v/v) against pore diameter (nm) for batch A using NMR cryoporometry and DSC thermoporometry.

The overall primary trend in the reduced tortuosity at higher molten fractions (above 0.6) can be assessed by comparison to various potential data models. Fig. 10 shows a comparison of the reduced tortuosity data for all samples of all batches together with the reciprocal relationship with molten fraction expected from the random cluster model described in the Theory section.

Fig. 11 shows log–log plots of fits of the data for all samples for each batch against an individual general power law data model for the variation of reduced tortuosity with molten fraction. The relevant statistics for the fits and the fitted power law exponents for each batch are shown in Table 5. The results of the F-tests suggest a good fit for all the data to a power law. From Table 5, it can be seen that the power law exponent for batch A is similar to unity, while those for batches C and D are close to unity, but marginally statistically-significantly lower, and that for batch B is still close to unity but statistically-significantly larger.

4.7. *Mercury porosimetry*

Fig. 12 shows the raw mercury porosimetry data for whole pellet samples from Batches A-D, obtained with an equilibration time of either 30 s or 100 s, following analysis with the modified Kloubek correlations given in the Theory section (Kloubek, 1981; Rigby, 2000). From Fig. 12, it can be seen that the application of the modified Kloubek correlations (Rigby, 2000) leads to a close superposition of the upper portions of the mercury intrusion and extrusion curves for all batches, and that any deviation is well within the experimental error arising from the calibration. This suggests that the modified Kloubek correlations (Rigby, 2000) have led to a removal of the effects of contact angle hysteresis. The residual hysteresis in the lower portions of the curves (for larger pore sizes) is, thus, probably due to structural hysteresis alone. It can also be seen that the form and position of the mercury intrusion curves for a given batch are independent of equilibration time. The extrusion curves for Batches B-D are also very similar for both equilibration times. The extrusion curves for 30 s and 100 s for Batch A are similar up to pore sizes of ~30 nm, and thereafter there is some deviation. The deviations between samples for Batch A might reflect some intra-batch variability.

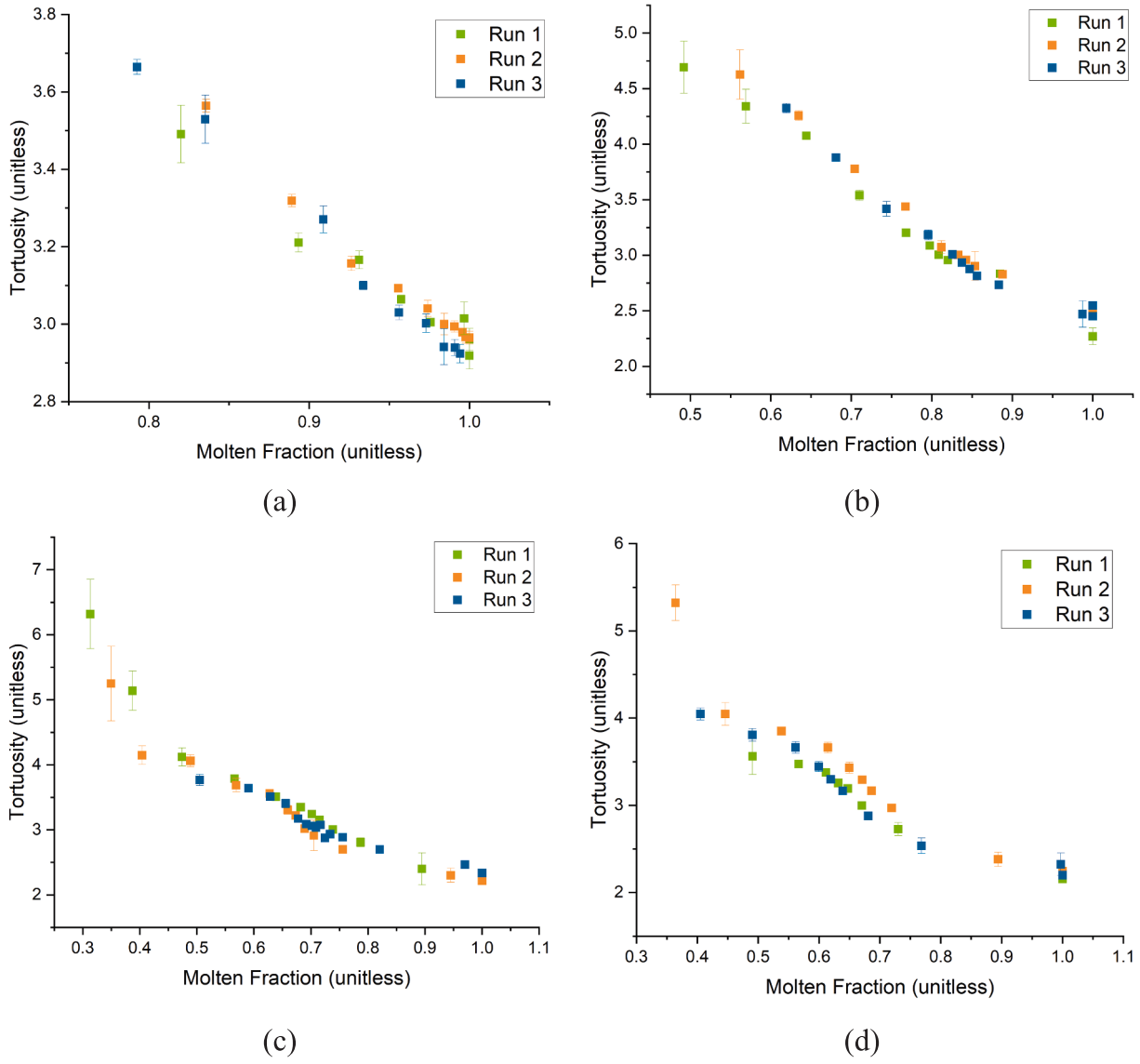

Fig. 8. Plots of tortuosity against molten fraction for batches A (a), B (b), C (c) and D (d). Each plot shows the data from 3 separate samples, with 3 different sets of pellets, for each batch with 95% confidence intervals on tortuosity.

For Batch A, with no induced macropores, the extrusion curve starts to deviate substantially from the intrusion curve beyond a pore size of ~7 nm. For Batches B-D, the point where the extrusion curve begins to deviate substantially from the intrusion curve has shifted to larger pores typically more around ~10 nm. Thereafter, for larger pores, the extrusion curve is virtually horizontal, thereby suggesting that almost all the mercury gets entrapped for pores larger than the deviation point between extrusion and intrusion curves. The values of mercury entrapment were calculated from the porosimetry curves shown in Fig. 12 and the values obtained are shown in Table 6. It can be seen that the best agreement between data for different equilibration times was for Batches C and D, and maybe Batch B too. However, there was a more significant difference for Batch A. The entrapment declines with increased equilibration time for Batch A, as might be expected from previous work (Rigby et al., 2008), as there is more time allowed for mercury to leave the sample between pressure decrements, and the typical pore neck-to-body ratio for Batch A is generally lower (as it has no large macropores) so less snap-off occurs.

4.8. Modelling

From the cryodiffusometry data, plots of the tortuosity against the largest molten diameter at the same temperature/molten volume fraction can be constructed and are shown in Fig. 13. For pore sizes below about 10 nm, there is a relatively rapid drop in tortuosity with increasing largest molten diameter, and thereafter the plot has a much gentler slope. This suggests that melting pores larger than about 10 nm does not improve the tortuosity relatively as much compared with the impact of melting pores below this value. The overall shape of these plots is similar to that observed by Forster et al. (Forster et al., 2020) for plots of tortuosity against average diameter obtained from PFG NMR experiments on fully molten *n*-octane in alumina catalyst supports with different average diameters. Forster et al. (Forster et al., 2020) grouped the alumina samples into two distinct regions with average diameters above and below a critical size at which the variation in self-diffusivity with average pore size changed dramatically. From Fig. 13, for batches B-D, if tangents are fitted to the data for the smaller and larger pore size intervals on either side of the sharp bend, then the critical pore size at the 'corner' of the plot can be identified as the intersection of the two fitted lines shown. Once this critical pore size has been identified in this

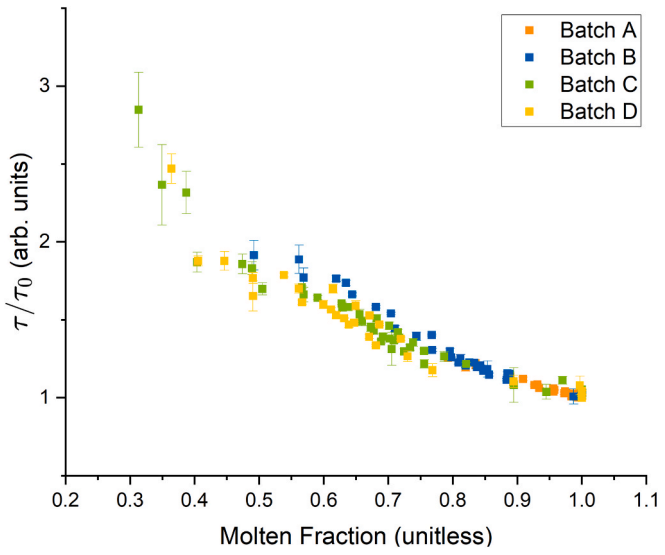

Fig. 9. Plots of reduced tortuosity against molten fraction for batches A–D.

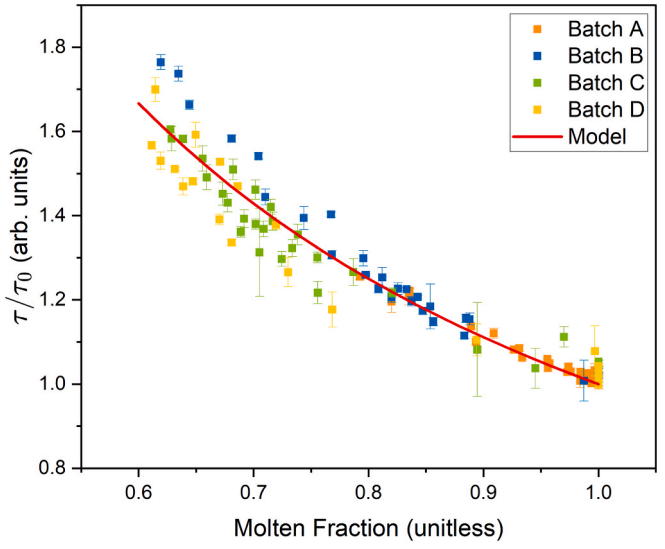

Fig. 10. Primary trend of reduced tortuosity against molten fraction (above a threshold of 0.60) for batches A-D, with the random cluster model fitted and shown as the red line.

manner, then the volume (molten) fraction of pores larger than this size can be found. The critical pore sizes and volume fractions thereby obtained for Batches B-D are shown in Table 7. The overall form of the plots in Fig. 13 is similar to what was anticipated using CPT in the Theory Section 2.5.

From Table 7, it is noted that, for each respective Batch, the molten fraction of pores larger than the critical size, identified from the linear constructions in Fig. 13, is similar to the mercury entrapment values shown in Table 6. It is also noted that the critical pore sizes are similar to the pore sizes (all ~10 nm) where the mercury porosimetry extrusion curve deviates substantially from the mercury intrusion curve in Fig. 12. The coincidence of the critical pore size for cryodiffusometry and mercury porosimetry was anticipated from CPT, as outlined in the Theory Section 2.5, and the latter, thus, provides an independent confirmation of the former. The critical pore sizes identified here from mercury porosimetry and cryoporometry are also similar to the critical pore sizes, for gaseous phase, Knudsen regime diffusion in the alumina matrix, identified in previous work (Collins et al., 2026), as might also be expected from CPT.

The tortuosity for self-diffusion of either water or cyclohexane in a fully molten sample was predicted from the random cluster model (Elias-Kohav et al., 1991), using Eq. (9), with the same total porosity as pellets from Batches A-D and compared with the experimental value in Fig. 14. This model prediction severely underestimates the experimental values for all Batches. However, also shown in Fig. 14 is the prediction from a modified random cluster model, using eq. (10), with the porosity calculated from the difference between the total pellet porosity and mercury entrapment from mercury porosimetry experiments conducted with an equilibration time of 30 s (from Table 6). From Fig. 14, it can be seen that the modified random cluster model gives rise to much better predictions of the measured tortuosity for both water and cyclohexane.

5. Discussion

A general decline in tortuosity with increased molten fraction was observed for all batches. This might be expected since the aforementioned typical rms displacements, during PFG experiments on partially molten samples, span length-scales encompassing the variation in the mesopore sizes, and, also, the typical spacing of the macropores, seen in the SEM and TEM images in Sections 4.1. and 4.2, respectively. In our previous work (Collins et al., 2026) on gas phase diffusion, it was observed that mesopore sizes were different in the boundary region of the macropores, compared with the mesoporous matrix, and that this may have restricted diffusion from the mesoporous matrix to the macropores. The hyperpolarised xenon MRI studies also suggested spatial heterogeneities in the spatial distribution of tortuosity (and likely pore size) (Collins et al., 2026). These observations might explain the extended nature of the molten fraction regions, and suggest why the observed tortuosity within a given molten region would be changed as the molten fraction increases and progressively more of the aforementioned features within them, or on their periphery, become molten too.

The mathematical form of the primary, overall trend in the experimental tortuosity against molten fraction curves, for larger molten fractions, is such that it follows very near to a reciprocal relationship, which suggests that the underlying geometry of the pore network is analogous to that of a random cluster, since the effect of addition of more porosity to the network follows that expected for ever more porous random clusters (RCs). The secondary effect of the short plateau-like regions of the melting curves for Batches B-D where the addition of extra molten porosity does not make much change to the tortuosity also hints at the presence of some “dead voidage” that does not make any apparent, observable contribution to the overall mass transfer rate.

However, the similarity, of the main trend in observed tortuosity with molten fraction, to a reciprocal relation might suggest another potential interpretation. If the water in the fully molten pores was in fast exchange with that in the non-freezing layer in still-frozen pores, then the observed PFG diffusivity, D_{obs}, would be a volume-weighted average of the diffusivity in the molten pores, D_M, and that in the non-freezing layer, D_{NFL}, such that:

$$D_{obs} = fD_M + (1-f)D_{NFL} \tag{11}$$

where f is the volume fraction of molten pores. If diffusion in the highly-confined non-freezing layer is much slower than in fully-molten pores such that $D_M \gg D_{NFL}$, then the variation in the observed tortuosity τ_{obs} with molten fraction would be approximately given by:

$$\tau_{obs} \approx \frac{\tau_M}{f}, \tag{12}$$

which is similar in mathematical form to what has been seen over some ranges of molten fraction. However, if this fast-exchange effect was operating, then it should continue to operate for all molten fractions, but, as the data in Figs. 8 and 9 show, the change in tortuosity plateaus/flattens (ie certainly deviates strongly from a simple reciprocal

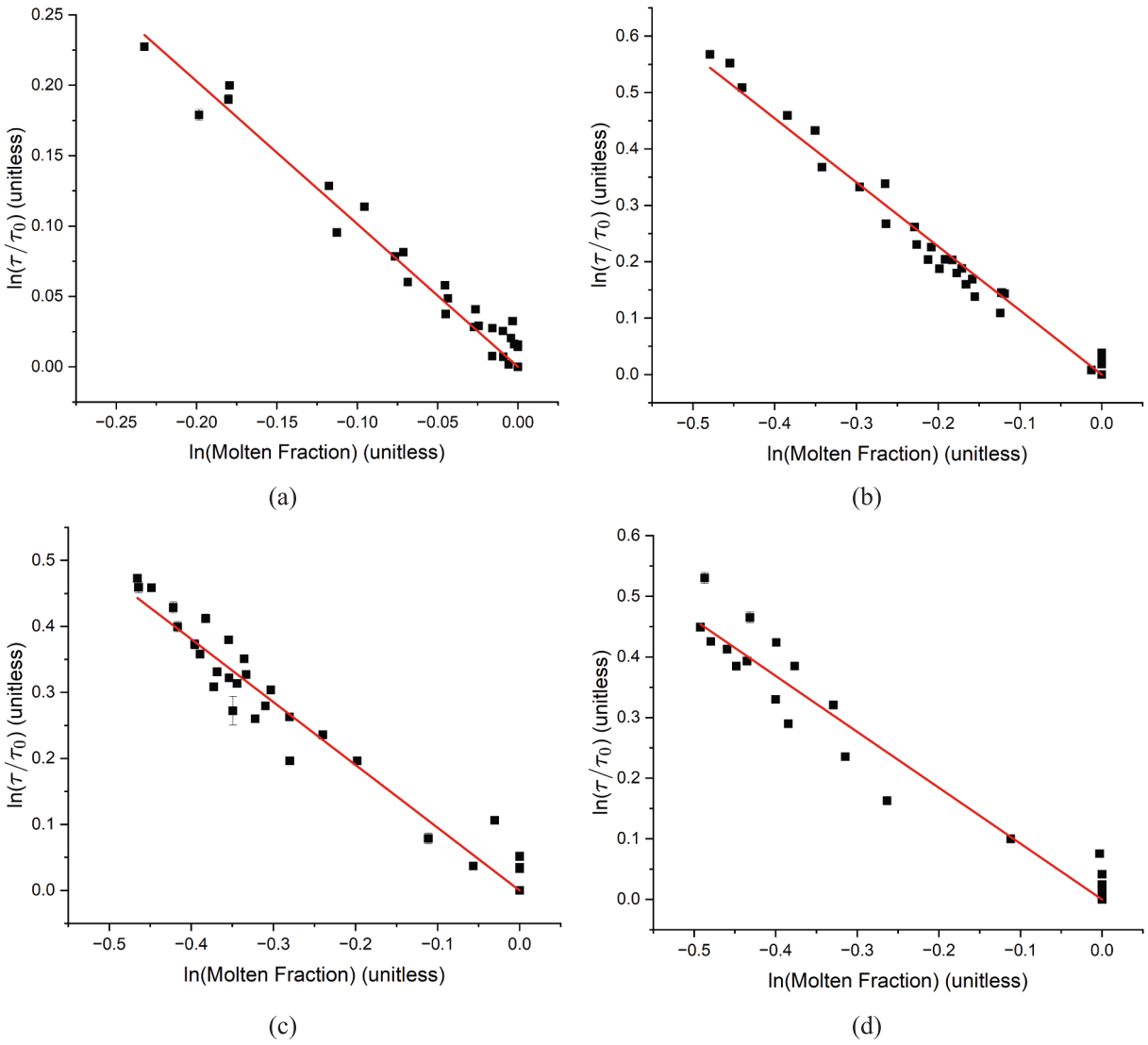

Fig. 11. Plots of power law data model fits (solid red lines) to the reduced tortuosity versus molten fraction data (■) for each batch A-D ((a)–(d), respectively).

Table 5
Results of the *F*-test and fitted parameters (with 95% confidence intervals) for power law data model fits to the reduced tortuosity versus molten fraction data for each batch A-D (in Fig. 11(a)–(d), respectively).

Batch	Power	Adjusted coefficient of determination, r^2	F-statistic	Significance
A	−1.01 ± 0.06	0.9388	1274	5.7×10^{-21}
B	−1.14 ± 0.04	0.9519	3707	6.4×10^{-27}
C	−0.95 ± 0.04	0.9492	2298	2.4×10^{-25}
D	−0.92 ± 0.06	0.9151	811.6	8.5×10^{-14}

relationship) between molten fractions from 0.4 to 0.6. The very presence of this behaviour is not consistent with the alternate interpretation of the trend elsewhere. Further, as mentioned above, this effect requires that the fully molten fraction and non-freezing layers would be in "fast exchange", but this is inconsistent with the observation of restricted diffusion, as implied by the form of the data in Fig. A2. Indeed, previous work (Petrov and Furó, 2011) has shown that such a barrier can occur. This previous study, performed on controlled pore glass, suggested that a closed surface existed between a large continuous molten region and the remaining frozen void space. The approximation that $D_{pore} \gg D_{NFL}$ may, also, not be fully self-consistent with the requirement for fast exchange between the phases. In addition, it is noted that the power-law exponents given in Table 5 are slightly, but statistically-significantly (outside 95% confidence intervals), different to the value of −1 expected from the simple reciprocal relationship in the alternative interpretation (and may suggest something more like a cluster–cluster aggregate (CCA) structure (see below)). If there was rapid exchange of water molecules between the fully molten pores and the non-freezing layer in still frozen pores, where the spin–lattice relaxation time is likely to be much shorter in the latter than the former, then the Brownstein-Tarr (Brownstein and Tarr, 1977) relaxation model would suggest a similar (to diffusion), simple reciprocal relation between the observed relaxation time and the frozen fraction (=1-molten fraction). However, as seen in the Appendix Fig. A3, this is not what has been observed for samples A-D. For samples B-D there is also a step up in relaxation time, as the macropores begin to melt, which would not be expected if the observed relaxation rate was dominated by the non-freezing layer in still-frozen pores. Further, in a log–log plot (see Fig. A3(b)) of relaxation time against frozen fraction, the slopes of the line segments fitted to the data above and below the steps are very far from a value of −1, and the fits are not good to a simple line, suggesting

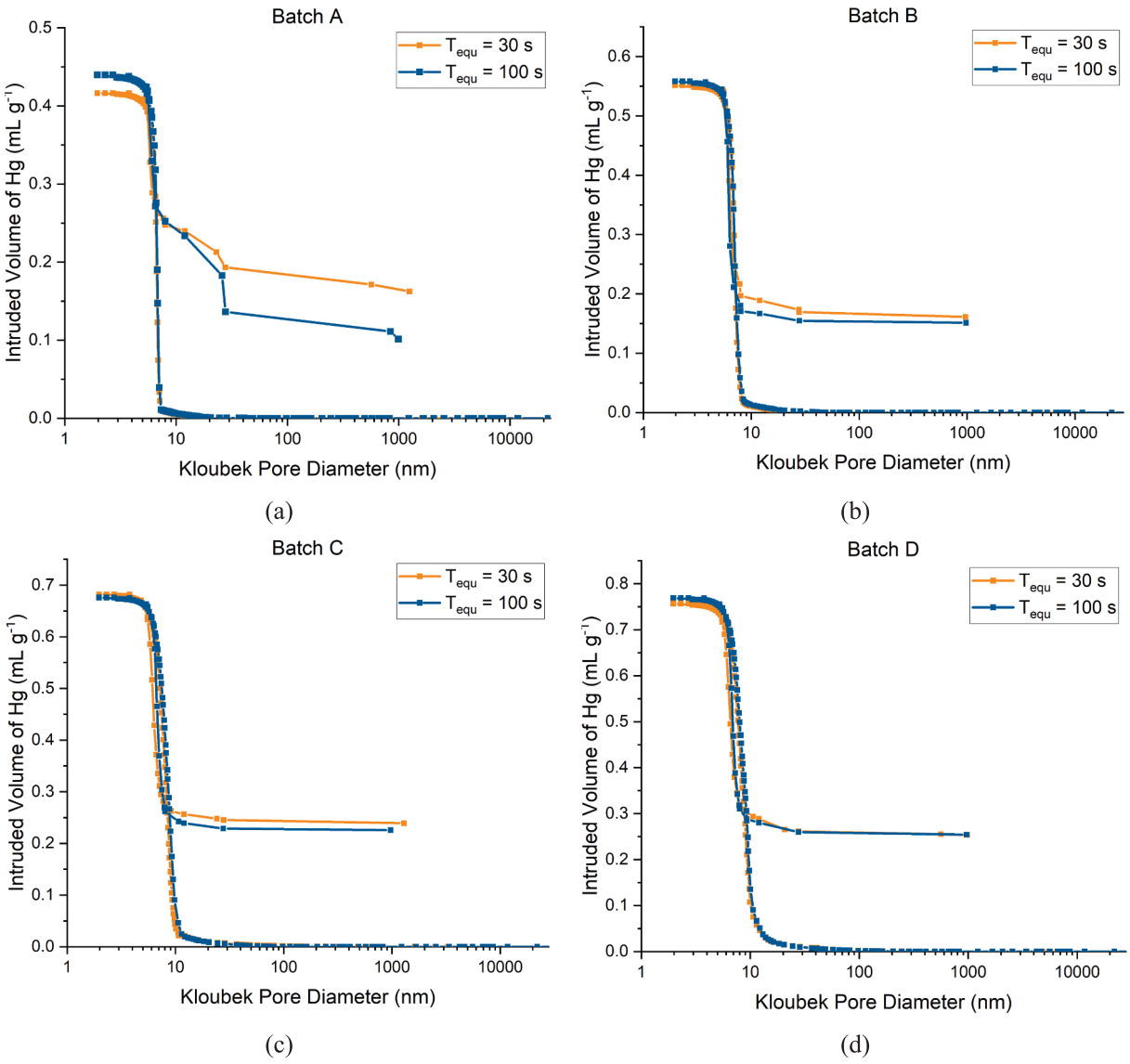

Fig. 12. Intruded mercury volume (mL g^{-1}) against the adjusted Kloubek pore diameter (nm), calculated using the modified Kloubek correlations at a given pressure (Kloubek, 1981), for the intrusion and extrusion of mercury at equilibration times of 30 and 100 s, for batches A (a), B (b), C (c) and D (d).

Table 6
Mercury porosimetry results for batches A-D, showing the average porosity and average fraction entrapment (v/v basis, dimensionless) with 95% confidence intervals, obtained from 3 repeats with different pellets, for equilibration times of 30 and 100 s.

Batch	T_{equ} = 30 s				T_{equ} = 100 s			
	Average Porosity		Fraction Entrapment		Average Porosity		Fraction Entrapment	
	Value	95% conf interval	Value	95% conf interval	Value	95% conf interval	Value	95% conf interval
A	0.582	0.004	0.365	0.022	0.580	0.016	0.243	0.024
B	0.613	0.025	0.293	0.002	0.620	0.033	0.265	0.010
C	0.678	0.010	0.343	0.009	0.672	0.019	0.334	0.004
D	0.698	0.015	0.339	0.010	0.704	0.002	0.332	0.003

more complex forms of variation than would be expected with exchange with the non-freezing layer. The slopes of the fitted lines in Fig. A3(b) also change significantly between before and after the step. Indeed, the size of the variation of spin–lattice relaxation time from before to after the step-up in Fig. A3(a) is what would be expected from the commencement of exchange between meso- and macro-pores, as melting of the macropores begins and continues. Hence, it seems unlikely that there is any significant exchange, between the bulk molten pores and the non-freezing layer in the still-frozen pores, over the timescales of the PFG or relaxation time experiments. This may also be hinted at by the two-component form of the log-attenuation data given in Fig. A1.

It has been seen that the level of apparent dead voidage can be measured using either the entrapment in mercury porosimetry, or (for Batches B-D) from suitable linear constructions applied to plots of tortuosity against maximum molten pore size obtained from the

(a)

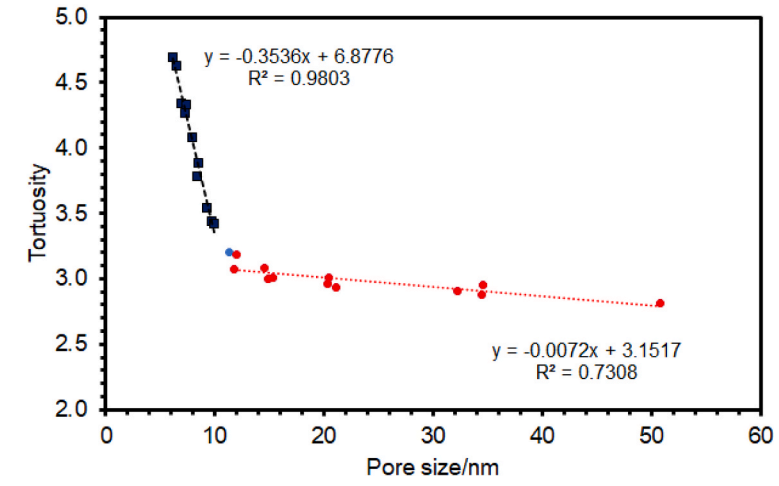

(b)

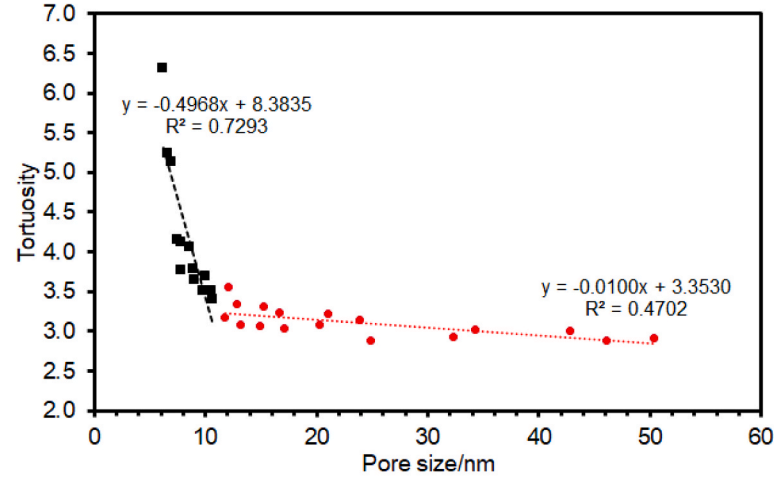

(c)

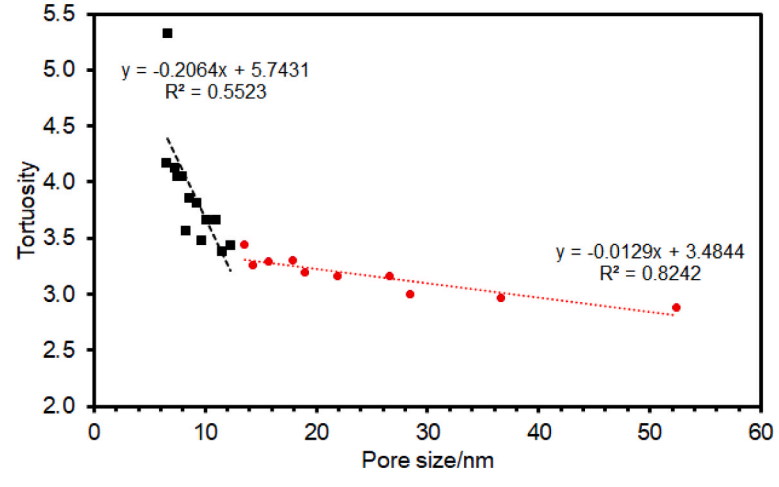

Fig. 13. Plot of tortuosity against largest molten pore diameter (at the same given molten fraction) for Batches (a) B, (b) C, and (c) D. The dashed and dotted lines, together with accompanying fitted equations, represent tangents fitted to the data for smaller (■) and larger (●) pore size intervals, respectively, either side of the sharp bend.

Table 7
Critical pores diameters extracted from the linear constructions in Fig. 13, and the volume fractions of pores larger than this, obtained from the cryoporometry melting curve, for Batches B–D.

Batch	Critical pore diameter/ nm	Molten fraction for pores larger than critical size
B	10.74	0.24
C	10.33	0.38
D	11.67	0.38

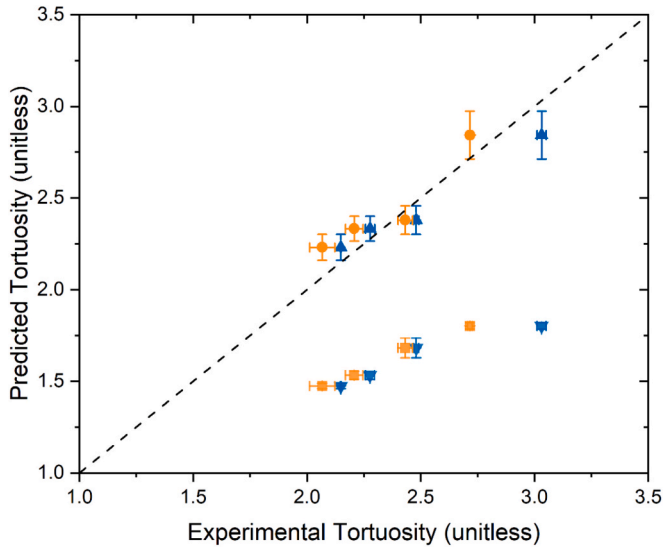

Fig. 14. Plot of experimentally measured tortuosity for water and cyclohexane versus the corresponding predictions of absolute tortuosity obtained from the standard random cluster (▼, water; ■, cyclohexane) and modified random cluster (▲, water; ●, cyclohexane) models for the total pellet porosity from mercury porosimetry, and from the useful porosity calculated from the mercury porosimetry data with an equilibration time of 30 s.

cryodiffusometry data. It has also been seen that the combination of these two main concepts, of a random cluster-like structural form together with the presence of some dead voidage, has led to good predictions of the tortuosity for fully molten samples. The analysis of the mercury porosimetry data with the modified Kloubek correlations (Kloubek, 1981) such that the upper parts of the intrusion and extrusion curves overlay each other, and so intrusion in the smallest pores is completely reversible, but diverge significantly only above a certain pore size, means that the entrapment occurs only in the largest mesopores and macropores, and, thence, this is the identity of the dead voidage. The saturation of entrapped mercury, given in Table 6, exceeds the macroporosity determined from the SEM, given in Table 3, and so some larger mesopores must also contain entrapped mercury. This is also in line with the observation that the values of frozen fraction (=1-molten fraction) at the step increases in spin–lattice relaxation time for batches B-D (given in Fig. A3), as the macropores begin to melt, are also just less than the fractional mercury entrapment for these batches.

Some previous diffusion modelling and simulation work by one of the authors (Rigby and Gladden, 1996) may shed some light on the origins of the aforementioned "dead voidage" effect. The modelling work involved modelling pore structures as three-dimensional (3D) cluster–cluster aggregate (CCA) fractals (Elias-Kohav et al., 1991). CCAs are formed by randomly modifying RC models until the solid forms a fully contiguous whole. In each time-step, of the simulation of the aggregation process, an individual, contiguous cluster of lattice sites designated as solid is selected at random, and that whole cluster is moved collectively one site along in a randomly chosen direction. If that cluster, thereby, makes nearest-neighbour contact with another solid cluster, then they are considered joined, and, thereafter, move as one. However, when the solid volume fraction of a RC exceeds the 3D site percolation threshold (of 0.312) for a simple cubic lattice, the amount of re-arrangement required such that all solid becomes contiguous with the percolating cluster is relatively small. Therefore, the re-arrangement to produce a 3D CCA from a 3D RC with a voidage fraction of 0.6 is relatively small, and the structures are very similar.

Hence, the tortuosity obtained previously from the whole object averaging method, which samples the whole void space evenly, for a 3D CCA with voidage fraction of 0.6 is ~1.7, which is similar to that expected from a RC using eq. (9) (of ~1.67). However, in previous work (Rigby and Gladden, 1996), it was also found that the tortuosity predicted, for a 3D CCA with a porosity of 0.6, from a random walk simulation method was of the order of 3, which was substantially higher than that obtained from the whole object averaging method and eq. (9). For a completely random cluster, the whole object averaging method gives the same tortuosity as eq.(9). For the random walk method, each walk of a particular length was repeated as many times as gives rise to a reasonable degree of random error (typically 10^4 random walking particles per path length) and was repeated for five to ten model clusters with the same void fraction. Hence, the observed tortuosity is an averaged value over many random walks.

It is noted that the tortuosity of ~3 for a CCA of porosity ~0.6 is similar to that obtained from PFG NMR for a fully-molten sample of Batch A above, which also has a similar voidage fraction (0.58 ± 0.02). In previous work (Rigby and Gladden, 1996), the difference in tortuosity between the random walk and whole object averaging methods was attributed to a difference in the sampling/averaging of the void space, whereupon the random walker did not visit all lattice sites. The random walker in the simulation could be like a self-diffusing water molecule in the PFG NMR experiment. Hence, the "dead volume" in the real alumina samples above is the poorly sampled regions of the void space. The CCA may be a good model for the structure of Batch A since the electron microscopy images show it is made up of aggregates of platelets, and the SAXS data suggests the aggregates may then agglomerate to form larger-scale structures. It is also noted that the particular sol–gel silica sphere samples with porosity of ~0.6, studied by Rigby and Gladden (Rigby and Gladden, 1996), that had measured tortuosities similar to the predictions of the whole object averaging method, have also been found to have zero mercury entrapment for fragmented samples (Rigby and Edler, 2002). Hence, for materials with little or no dead volume the total porosity and random cluster can predict the liquid-phase tortuosity from PFG NMR.

It is noted that the apparent connectivity obtained from nitrogen sorption scanning curves that filled pores up to ~14 nm was higher than for scanning curves that filled pores up to ~50 nm. This suggested that the sub-network of smaller mesopores was relatively more accessible than the mesopore network that also contained the larger mesopores above ~14 nm in size. Hence, the larger mesopores are probably much less accessible than the smaller mesopores as they bring the overall connectivity down. Lower pore network connectivity is also generally associated with higher mercury entrapment (Rigby, 2020; Wardlaw and McKellar, 1981; Tsakiroglou and Payatakes, 1998), and thus the much greater entrapment in larger pores is also consistent with this finding. If the smaller mesopores are more accessible they are likely to facilitate easier mass transport exchange. This is consistent with the NMR cryodiffusometry data in Fig. 13 that suggested the smaller mesopores had a greater impact on the rate of self-diffusion of water within the molten network than mesopores larger than the critical sizes in Table 7, which are similar to 14 nm. It has been shown that the "dead voidage" is mainly coming from the macropores which is counterintuitive because, at first, it's usually small mesopores which are, typically, thought to make less contribution to mass transport. However, the TEM data may offer an explanation for this counterintuitive result, as it shows that there is a potential barrier to efficient diffusion in the mesoporous region at the boundary of the macropores in the form of the aligned alumina platelets

arranged with their long axes parallel to the boundary, thereby restricting diffusion to the small gaps at the ends of the platelets.

The comparison of the PFG NMR tortuosities for water and cyclohexane, generally showing a small difference between the two, suggests that the water tortuosity probably only contains a small contribution from interactions with the surface since hydrocarbons generally have much weaker interactions with polar surfaces like alumina (D'Agostino et al., 2012). The relative similarity of the sets of values of tortuosity for water and cyclohexane for either standard RCs or modified RCs, but the much bigger difference for both fluids between standard RCs and modified RCs, in Fig. 14, suggests that the impact of any differences in surface interactions on diffusion for the fully molten samples is much smaller than the so-called "dead volume" effect. Given that the same primary trend in the variation of reduced tortuosity with molten fraction, seen in Fig. 10, and the power laws seen in Fig. 11, are maintained over the wide range of molten fractions from 1.0 down to 0.6, then this suggests that there is no substantial additional effect of alumina surface interactions with water intruding as the molten phase is confined to ever smaller pores for the range of sizes tested. If there was increased surface interaction with greater confinement, then a systematic deviation from the trendlines towards higher tortuosity would be expected with decreasing molten fraction, but a significant such effect is not seen.

6. Conclusions

The characterisation techniques presented here provide a superior assessment, to previous work, of the impact of introducing macroporosity by the porogen-based method (Rigby, 2020; Yang et al., 2024; Santos et al., 2022; Isaacs et al., 2019; Müllner et al., 2016; Ghanbarian et al., 2013; Bukowski et al., 2021; Holzer et al., 2023). Electron microscopy and SAXS data have demonstrated the complex, hierarchical nature of the pore structure of porogen-templated, bidisperse alumina pellets. NMR cryodiffusometry has been used to implement the so-called "sifting strategy" and, thereby, can identify the key aspects of the void space to include in a minimalist, pore structural model. This strategy has been shown to be superior to alternatives, using the so-called "brute-force" approach, for complex hierarchical pore structures, as studied here. Critical path theory-based analysis of the cryodiffusometry data suggested that the addition of macroporosity via the porogen method led to some increase in the critical pore size but it remained mesopore-sized. The particular mathematical form of the cryodiffusometry data showed that the overall geometry of the void space was akin to that of a random cluster, but also, additionally, detected the presence of so-called "dead volume" regions that apparently provided little, or no, contribution to the overall mass transport. The presence of the dead volume was confirmed via mercury retraction porosimetry, and demonstrated, via seeded percolation analysis of nitrogen sorption scanning curves, to be associated with particular pores of poor accessibility through relatively low connectivity. The importance of relative sampling of particular void space regions, for their contribution to overall observed mass transport rates, was further demonstrated via a comparison with Monte-Carlo random walk simulations of tracer migration on random cluster models. This effect may have been facilitated in the alumina pellets by the surface barrier of the aligned platelets occurring at the boundary with the macropores seen in the TEM images. Overall, the RC structural model with dead volume explained more of the diverse experimental findings than the CPT framework. These findings, thus, suggest that the alumina synthesis concomitantly results in the formation of dead volume, and this is the controlling factor determining liquid-phase mass transport properties.

CRediT authorship contribution statement

Stefano Collins: Writing – original draft, Methodology, Investigation. **Dina Lofficial:** Writing – original draft, Supervision, Resources, Project administration, Methodology, Investigation, Funding acquisition, Conceptualization. **Séverine Humbert:** Writing – original draft, Methodology, Investigation, Data curation. **Thibaud Chevalier:** Methodology, Investigation, Data curation. **Christophe Vallee:** Writing – original draft, Supervision, Resources, Project administration, Methodology, Investigation, Funding acquisition, Conceptualization. **Huw E.L. Williams:** Writing – original draft, Supervision, Resources, Project administration, Methodology, Investigation, Data curation, Conceptualization. **Galina E. Pavlovskaya:** Writing – original draft, Supervision, Resources, Project administration, Methodology, Investigation, Funding acquisition, Data curation, Conceptualization. **Thomas Meersmann:** Writing – original draft, Supervision, Resources, Project administration, Methodology, Investigation, Funding acquisition, Conceptualization. **Sean P. Rigby:** Writing – review & editing, Writing – original draft, Validation, Supervision, Resources, Project administration, Methodology, Investigation, Funding acquisition, Data curation, Conceptualization.

Declaration of competing interest

The authors declare that they have no known competing financial interests or personal relationships that could have appeared to influence the work reported in this paper.

Acknowledgments

SC, SPR, HELW, GEP and TM thank IFPEN for the provision of the PhD studentship for SC.

Appendix A

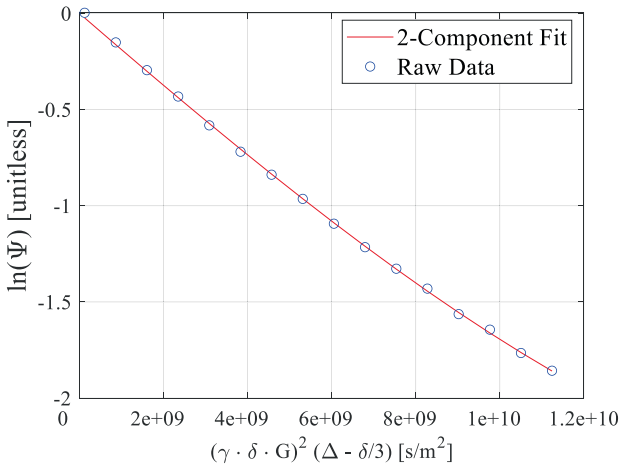

Fig. A1. Example PFG NMR attenuation curve fitted to the bi-exponential model. The fit yields: $D_1 = 2.01 \times 10^{-10}$ m^2/s, $D_2 = 2.22 \times 10^{-22}$ m^2/s and $p_1 = 0.94$. Sample information: Batch D, Run 3, Temperature = 267.1 K, $\Delta = 0.1$ s.

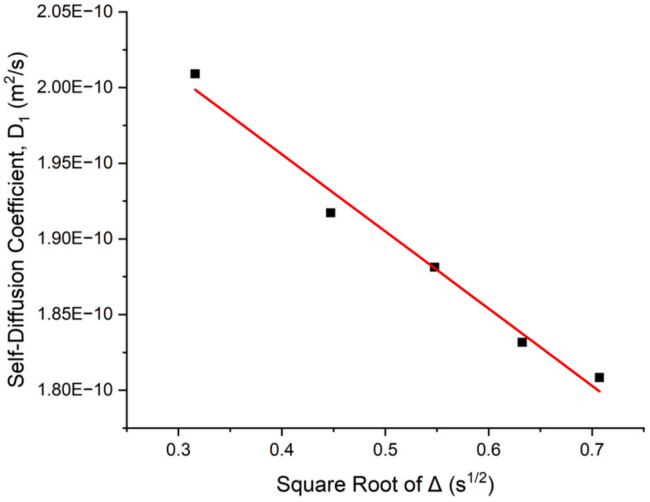

Fig. A2. Example plot of the measured diffusivity (fast diffusing component, D_1) against the square root of the diffusion time, $\Delta^{1/2}$, fitted to a regression model with a line of best fit in red. Fit results: $D_0 = (2.16 \pm 0.04) \times 10^{-10}$ m^2/s. Sample information: Batch D, Run 3, Temperature = 267.1 K, molten fraction 0.49. The range in rms displacements for the diffusivity D_0, over the range of diffusion times probed, corresponds to 10 to 25 μm. The value of V/S from the fit shown corresponds to 40 μm.

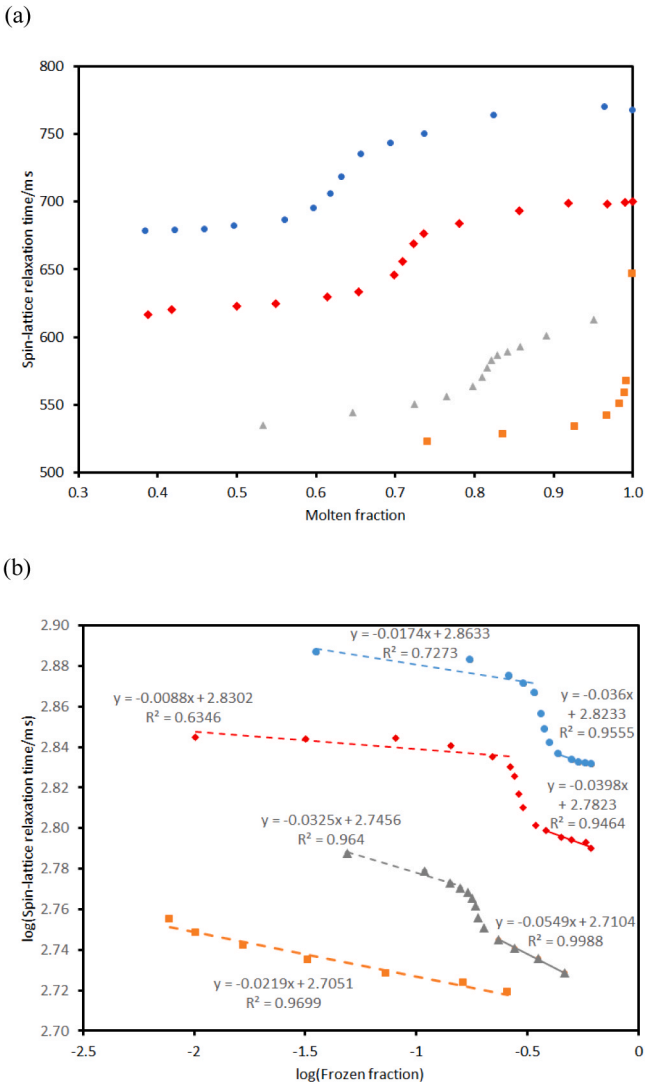

Fig. A3. (a) Variation of spin lattice relaxation time with molten fraction for batches A (■), B (▲), C (◆) and D (●). (b) Variation of the logarithm of spin lattice relaxation time with the logarithm of the frozen fraction (=1-molten fraction) for batches A, B, C and D. The lines shown are straight-line fits to the segments above and below the steps.

Appendix B. Supplementary data

Supplementary data to this article can be found online at https://doi.org/10.1016/j.ces.2026.123752.

Data availability

The data that has been used is confidential.

References

Ambegoakar, V., Halperin, N.I., Langer, J.S., 1971. Hopping conductivity in disordered systems. Phys. Rev. B Solid State 4, 2612–2620.
Appel, M., Stallmach, F., Thomann, H., 1998. Irreducible fluid saturation determined by pulsed field gradient NMR. J. Petrol. Sci. Engng. 19, 45–54.
Bafarawa, B., Nepryahin, A., Ji, L., Holt, E.M., Wang, J., Rigby, S.P., 2014. Combining mercury thermoporometry with integrated gas sorption and mercury porosimetry to improve accuracy of pore-size distributions for disordered solids. J. Colloid Interface Sci. 426, 72–79.
Brownstein, K.R., Tarr, C.E., 1977. Spin-lattice relaxation in a system governed by diffusion. J. Magn. Reson. 26, 17–25.
Bukowski, B.C., Keil, F.J., Ravikovitch, P.I., Sastre, G., Schnurr, R., Coppens, M.-O., 2021. Connecting theory and simulation with experiment for the study of diffusion in nanoporous solids. Adsorption 27, 683–760.
Collins, S., Humbert, S., Lofficial, D., Vallee, C., Parmenter, C., Williams, H.E.L., Harrison, A., Filkins, M., Pavlovskaya, G.E., Meersmann, T., Rigby, S.P., 2026. Hyperpolarized Xenon-129 MRI, Fluorine-19 PFG NMR, SAXS and electron microscopy studies of the impact on structure and gas phase mass transport of introducing controlled macroporosity into mesoporous, alumina, catalyst support pellets. Chem. Eng. Sci. 321B, 122843.
D'Agostino, C., Mitchell, J., Gladden, L.F., Mantle, M.D., 2012. Hydrogen bonding network disruption in mesoporous catalyst supports probed by PFG-NMR diffusometry and NMR relaxometry. J. Phys. Chem. C 116, 8975–8982.
A. A.Deshmukh, S.S. Deshmukh, S.S. Salgaonkar, G. Sethia, Alumina and alumina extrudates and process for preparation thereof, US10576457B2, (2018).
Dong, B., Wang, L., Min, Z., Wang, Q., Yin, C., Jia, T., Wang, Y., Zheng, X., Wang, F., Abadikhah, H., Xu, X., Zhang, Y., Gang, G., 2022. Fabrication of novel porous Al2O3 substrates by combining emulsion templating and gel-tape-casting methods. Ceram. Int. 48, 7320–7734.
Dore, J., Weber, B., Strange, J., Farman, H., Descamps, M., Carpenter, L., 2004. Phase transformations for cyclohexane in mesoporous silicas. Physica A 333, 10–16.
Dullien, F.A.L., 1992. Porous Media: Fluid Transport and Pore Structure, 2nd ed. Academic Press, San Diego.
Kikkinides, E.S., Valiullin, R., 2023. A new statistical theory for constructing sorption isotherms in mesoporous structures represented by Bethe lattices. Chem. A Eur. J. 127, 8734–8750.

Elias-Kohav, T., Sheintuch, M., Avnir, D., 1991. Steady-state diffusion and reactions in catalytic fractal porous media. Chem. Eng. Sci. 46, 2787–2798.
Filippov, A.V., Skirda, V.D., 2000. An investigation of the structure of a porous substance by NMR cryodiffusometry. Colloid J. 62, 759–764.
Forster, L., Lutecki, M., Fordsmand, H., Le, Yu., D'Agostino, C., 2020. Tailoring morphology of hierarchical catalysts for tuning pore diffusion behaviour: a rational guideline exploiting bench-top pulsed-field gradient (PFG) nuclear magnetic resonance (NMR). Mol. Syst. Des. Eng. 5, 1193–1204.
Friedman, S.P., Seaton, N.A., 1998. Critical path analysis of the relationship between permeability and electrical conductivity of three-dimensional pore networks. Water Resour. Res. 34, 1703–1710.
Ghanbarian, B., Hunt, A.G., Ewing, R.P., Sahimi, M., 2013. Tortuosity in porous media: a critical review. Soil Sci. Soc. Am. J. 77, 1461–1477.
Giesche, H., 2006. Mercury porosimetry: a general (practical) overview. Part. Part. Syst. Char. 23, 9–19.
Gjerdåker, L., Humborstad Sørland, G., Aksnes, D., 1999. Application of the short diffusion time model to diffusion measurements by NMR in microporous crystallites. Microporous Mesoporous Mater. 32, 305–310.
Gregg, S.J., Sing, K.S.W., 1982. Adsorption, Surface Area and Porosity. Academic Press Inc, London.
Hill-Casey, F., Hotchkiss, T., Hardstone, K.A., Hitchcock, I., Novak, V., Schlepütz, C.M., Meersmann, T., Pavlovskaya, G.E., Rigby, S.P., 2021. Hyperpolarised xenon MRI and time-resolved X-ray computed tomography studies of structure-transport relationships in hierarchical porous media. Chem. Eng. J. 405, 126750.
Hollewand, M.P., Gladden, L.F., 1995. Transport heterogeneity in porous pellets-I. PGSE NMR studies. Chem. Engng. Sci. 50, 309–326.
Holzer, L., Marmet, P., Fingerle, M., Wiegmann, A., Neumann, M., Schmidt, V., 2023. Tortuosity and Microstructure Effects in Porous Media: Classical Theories, Empirical Data and Modern Methods. Springer International Publishing, Cham.
Isaacs, M.A., Robinson, N., Barbero, B., Durndell, L.J., Manayil, J.C., Parlett, C.M.A., D'Agostino, C., Wilson, K., Lee, A.F., 2019. Unravelling mass transport in hierarchically porous catalysts. J. Mater. Chem. A 7, 11814–11825.
Jia, Y., Hazra, R., Wu, A., Patel, S.M., Gadikota, G., 2025. Mechanisms underlying the freezing and melting behavior of water confined in silica nanopores as a function of pore size and pore filling. PCCP 27, 19465–19479.
Kloubek, J., 1981. Hysteresis in porosimetry. Powder Technol. 29, 63–73.
Kolitcheff, S., Jolimaitre, E., Hugon, A., Verstraete, J., Carrette, P.-L., Tayakout-Fayolle, M., 2017. Tortuosity of mesoporous alumina catalyst supports: Influence of the pore network organization. Microporous Mesoporous Mater. 248, 91–98.
Kondrashova, D., Dvoyashkin, M., Valiullin, R., 2011. Structural characterization of porous solids by simultaneously monitoring the low-temperature phase equilibria and diffusion of intrapore fluids using nuclear magnetic resonance. New J. Phys. 13, 015008.
Lakshmi, D.S., Radha, K.S., Castro-Muñoz, R., Tańczyk, M., 2022. Emerging trends in porogens toward material fabrication: recent progresses and challenges. Polymers 14, 5209.
Larson, R.G., Scriven, L.E., Davis, H.T., 1981. Percolation theory of two phase flow in porous media. Chem. Engng Sci. 36, 57–73.
Liabastre, A.A., Orr, C., 1978. Evaluation of pore structure by mercury penetration. J. Colloid Interface Sci. 64, 1–18.
Mitra, P.P., Sen, P.N., Schwartz, L.M., 1993. Short time behaviour of the diffusion coefficient as a geometrical probe of porous media. Phys. Rev. B 47, 8565–8574.
Mousa, S., Baron, K., Fletcher, R.S., Rigby, S.P., 2022. Triangulation of pore structural characterisation of disordered mesoporous silica using novel hybrid methods involving dual-probe porosimetries. Colloids Surf. A: Phys. Eng Aspects 653, 130026.
Mousa, S., Novak, V., Fletcher, R.S., Garcia, M., Mcleod, N., Corfield, M., Rigby, S.P., 2023. Integration of multi-scale porosimetry and multi-modal imaging in the study of structure-transport relationships in porous catalyst pellets. Chem. Eng. J. 452, 139122.
Mousa, S., Novak, V., Fletcher, R.S., Kelly, G., Garcia, M., Mcleod, N., Parmenter, C., Rigby, C.S.P., 2023. Evolution of the pore structure-transport relationship during catalyst reduction and sintering studied by integrated multi-scale porosimetry and multi-modal imaging. Chem. Eng. Sci. 277, 118880.
Müllner, T., Unger, K.K., Tallarek, U., 2016. Characterization of microscopic disorder in reconstructed porous materials and assessment of mass transport-relevant structural descriptors. New J. Chem. 40, 3993–4015.
Nepryahin, A., Fletcher, R.S., Holt, E.M., Rigby, S.P., 2016. Structure-transport relationships in disordered solids using integrated rate of gas sorption and mercury porosimetry. Chem. Eng. Sci. 152, 663–673.
Parlar, M., Yortsos, Y.C., 1988. Percolation theory of vapour adsorption desorption processes in porous materials. J. Colloid Interface Sci. 124, 162–176.
Pavlovskaya, G.P., Meersmann, T., Jin, C., Rigby, S.P., 2018. Fluid flow in a porous medium with transverse permeability discontinuity. Phys. Rev. Fluids 3, 044102.
Perkins, E.L., Lowe, J.P., Edler, K.J., Tanko, N., Rigby, S.P., 2008. Determination of the percolation properties and pore connectivity for mesoporous solids using NMR cryodiffusometry. Chem. Eng. Sci. 63, 1929–1940.
Petrov, O., Furó, I., 2006. Curvature-dependent metastability of the solid phase and the freezing-melting hysteresis in pores. Phys. Rev. E 73, 011608.
Petrov, O.V., Furó, I., 2009. NMR cryoporometry: Principles, applications and potential. Prog. Nucl. Magn. Reson. Spectrosc. 54 (2), 97–122. https://doi.org/10.1016/j.pnmrs.2008.06.001.
Petrov, O., Furó, I., 2011. A study of freezing-melting hysteresis of water in different porous materials. Part I: porous silica glass. Micropor. Mesopor. Mater. 138, 221–227.
Rigby, S.P., 2000. New methodologies in mercury porosimetry. Stud. Surf. Sci. Catal. 144, 185–192.
Rigby, S.P., 2020. Structural Characterisation of Natural and Industrial Porous Materials: a Manual. Springer International Publishing, Cham.
Rigby, S.P., 2023. The anatomy of amorphous, heterogeneous catalyst pellets. Materials 16, 3205.
Rigby, S.P., Chigada, P.I., Evbuomvan, I.O., Chudek, J.A., Miri, T., Wood, J., Bakalis, S., 2008. Experimental and modelling studies of the kinetics of mercury retraction from highly confined geometries during porosimetry in the transport and the quasi-equilibrium regimes. Chem. Eng. Sci. 63, 5771–5788.
Rigby, S.P., Edler, K.J., 2002. The influence of mercury contact angle, surface tension and retraction mechanism on the interpretation of mercury porosimetry data. J. Colloid Interface Sci. 250, 175–190.
Rigby, S.P., Gladden, L.F., 1996. NMR and fractal modelling studies of transport in porous media. Chem. Eng. Sci. 51, 2263–2272.
Rigby, S.P., Watt-Smith, M.J., Fletcher, R.S., 2004. Simultaneous determination of the pore-length distribution and pore connectivity for porous catalyst supports using integrated nitrogen sorption and mercury porosimetry. J. Catal. 227, 68–76.
Santos, V., Chang, B., Gigliotti, A., Yin, Y., Song, W., Prodanović, M., Kang, O., Lubbers, N., Viswanathan, H.A., 2022. Dataset of 3D structural and simulated transport properties of complex porous media. Sci. Data 9, 579.
Schreiber, A., Ketelsen, I., Findenegg, G.H., 2001. Melting and freezing of water in ordered mesoporous silica materials. Phys. Chem. Chem. Phys. 3, 1185–1195.
Seaton, N.A., 1991. Determination of the connectivity of porous solids from nitrogen sorption measurements. Chem. Eng. Sci. 46, 1895–1909.
Shiko, E., Edler, K.J., Lowe, J.P., Rigby, S.P., 2012. Probing the impact of advanced melting and advanced adsorption phenomena on the accuracy of pore size distributions from cryoporometry and adsorption using NMR relaxometry and diffusometry. J. Colloid Interface Sci. 385, 183–192.
Söllner, J., Neimark, A.V., Thommes, M., 2024. Development and application of an advanced percolation model for pore network characterization by physical adsorption. Langmuir 40, 23146–23168.
Tsakiroglou, C.D., Payatakes, A.C., 1998. Mercury intrusion and retraction in model porous media. Adv. Colloid Interface Sci. 75, 215–253.
Twigg, M.V., 2014. The Catalyst Handbook, second ed. CRC Press, Taylor & Francis Group, Boca Raton, FL.
Van Brakel, J., Modrý, S., Svatá, M., 1981. Mercury porosimetry: state of the art. Powder Technol. 29, 1–12.
Wakao, W., Smith, J.M., 1963. Diffusion in catalyst pellets. Chem. Eng. Sci. 17, 825–834.
Wardlaw, N.C., McKellar, M., 1981. Mercury porosimetry and the interpretation of pore geometry in sedimentary rocks and artificial models. Powder Technol. 29, 127–143.
Washburn, E.W., 1921. The dynamics of capillary flow. Phys. Rev. 17, 273–283.
Yamada, H., Tagawa, T., Nagao, S., Kato, S., 2021. Investigation of gas diffusion phenomena in porous catalyst support pellets based on microstructure. Catal. Today 375, 30–35.
Yang, G., Xu, R., Tian, Y., Guo, S., Wu, J., Chu, X., 2024. Data-driven methods for flow and transport in porous media: a review. Int. J. Heat & Mass Transfer 235, 126149.